Chapter 1
A Topological Approach to Vortex Knots and Links

Xin Liu, Renzo L. Ricca, and Hao Guan

Abstract Here we review some recent developments in the topological study of vortex knots and links. We start from fundamental properties of kinetic helicity, a conserved quantity of ideal fluid mechanics, focusing on the topological interpretation in terms of linking numbers. Then we proceed to consider the derivation from helicity of the Jones and HOMFLYPT knot polynomials, showing that their adapted formulation can be expressed in terms of writhe and twist helicity. Through explicit computations and examples, we also show that these adapted polynomials provide useful information to quantify the topological cascade of reconnecting vortex knots and links in relation to energy. In an effort to establish direct relationships between topological complexity and energy contents, we highlight the role of ropelength in the energy relaxation of magnetic knots. Optimal pathways of decaying vortex knots are re-considered by a new approach based on the interpretation of geodesic flows in an appropriate knot polynomial space. This novel approach proves to be useful to determine the probability associated with each topological state, and the topological degeneration of fluid structures undergoing a change of topology. As an example, we consider the numerical simulation of the decay of 3 vortex loops linked together to form a system of Borromean rings. The evolution of such system is governed by

X. Liu (✉) · H. Guan
Institute of Theoretical Physics, Faculty of Sciences, Beijing University of Technology, Beijing, P.R. China
e-mail: xin.liu@bjut.edu.cn

R. L. Ricca
Department of Mathematics and Applications, University of Milano-Bicocca, Milan, Italy
e-mail: renzo.ricca@unimib.it

R. L. Ricca, X. Liu (eds.), *Knotted Fields*, Lecture Notes in Mathematics 2344,
https://doi.org/10.1007/978-3-031-57985-1_1

the Gross-Pitaevskii equation, and preliminary results of this test case are analysed in terms of energy transfers.

1.1 Helicity and Linking Numbers of Fluid Knots and Links

A central task of topological fluid mechanics is to determine the role of topological information in the evolution and energetics of complex fluid structures. This approach offers powerful techniques to determine new relations between energy and structural complexity particularly when localised fields form knots and links. In this context helicity is the most important topological property of fluid flows; it is a conserved quantity of the Euler's equation, and it is a robust invariant under the dissipative Navier-Stokes equations. The study of the topological implications of helicity, and its role in relation to energy, are central topics of modern research in fluid mechanics [32].

The importance of topological aspects of fluid flows is highlighted by Helmholtz's conservation laws (1858), and it was exploited by Kelvin in his vortex atom theory [52] by providing a mathematical justification for the discrete energy spectra of chemical elements. But it took more than 100 years with the seminal work of Moffatt [30], to realise that the helicity of fluid flows (a quantity whose conservation was discovered by Woltjer [55] and Moreau [35]), had a topological meaning when vortex and magnetic fields form complex structures.

In 1984 Berger and Field considered the decomposition of magnetic helicity of a finite number of isolated flux tubes, to analyse the relationship between this quantity and the geometry and topology of the constituent field lines [8]. In recent years, researchers made further progress in the theoretical and numerical analysis of the helicity contributions in real viscous flows [33, 56], as well as in the experimental measures of its effects [48].

In the case of vortical flows the *kinetic helicity* is defined as a 3D volume integral [35]:

$$H = \int_V \boldsymbol{u} \cdot \boldsymbol{\omega} \, \mathrm{d}^3\boldsymbol{x} \ , \tag{1.1}$$

where $\boldsymbol{u}$ is the velocity, and $\boldsymbol{\omega} = \nabla \times \boldsymbol{u}$ the vorticity in the fluid volume V, with no-flux condition on the boundary, i.e. $\boldsymbol{\omega} \cdot \hat{\boldsymbol{n}} = 0$ on ∂V ($\hat{\boldsymbol{n}}$ unit normal to ∂V). For incompressible flows we have the condition $\nabla \cdot \boldsymbol{u} = 0$, i.e. $\boldsymbol{u}$ is divergence-free everywhere in V. For compressible flows, $p = p(\rho)$, where p denotes pressure, and ρ fluid density. The magnetic helicity is defined similarly, by replacing $\boldsymbol{u}$ with the magnetic vector potential $\boldsymbol{A}$, and $\boldsymbol{\omega}$ with the magnetic field $\boldsymbol{B}$. Without loss of generality, and for simplicity, here we will simply refer to kinetic helicity.

In terms of the basic field $\boldsymbol{\omega}$, one can re-write the definition (1.1) as

$$H = \int_V \mathrm{curl}^{-1}\boldsymbol{\omega} \cdot \boldsymbol{\omega} \, \mathrm{d}^3\boldsymbol{x} \ , \tag{1.2}$$

where $\boldsymbol{u} = \text{curl}^{-1}\boldsymbol{\omega}$ is derived from the *Biot-Savart formula*

$$\boldsymbol{u}(\boldsymbol{x}) = \frac{1}{4\pi}\int_V \frac{\boldsymbol{\omega}\left(\boldsymbol{x}'\right)\times\left(\boldsymbol{x}-\boldsymbol{x}'\right)}{|\boldsymbol{x}-\boldsymbol{x}'|^3}\,\mathrm{d}^3\boldsymbol{x}'\,. \tag{1.3}$$

Equation (1.2) highlights the fact that H depends on $\boldsymbol{\omega}$ rather than $\boldsymbol{u}$ (see [1], Theorem 1.15). From a theoretical viewpoint the divergence-free $\boldsymbol{\omega}$ plays the role of a gauge field given by an observable quantity, while $\boldsymbol{u}$ plays the role of a gauge potential. Notice that the importance of gauge potentials was fully recognised only in the last decades, after the realisation of the Aharonov-Bohm (AB) effect.

As regards Eq. (1.2), one has the following fundamental theorem.

Theorem 1.1 ([1]) *Let $\boldsymbol{\omega}$ be a divergence-free vector field defined on a manifold $\mathcal{M}$. The helicity H of $\boldsymbol{\omega}$ is conserved under an arbitrary, volume-preserving diffeomorphism of $\mathcal{M}$.*

The theorem states that for a simply-connected manifold $\mathcal{M}$, if a vector field $\boldsymbol{u}$ on $\mathcal{M}$ is divergence-free and tangent to the boundary $\partial\mathcal{M}$, then the helicity H is an invariant under all possible volume-preserving diffeomorphisms of $\mathcal{M}$. Proof of the theorem is a direct result of the Cauchy solutions to the Helmholtz's equations, and of Moreau's derivation. From a topological viewpoint H can be interpreted as a Hopf invariant in terms of the degree of a Hopf map [1].

1.1.1 Linking Number Interpretation of Helicity

For fields localised in flux tubes forming knots and links Moffatt [30] and Moffatt and Ricca [34, 43] gave a rigorous interpretation of helicity in terms of mutual and self-linking numbers. Consider an N-component vortex link $\mathcal{L} = \bigsqcup_{i=1}^{N}\gamma_i$, where γ_i denotes the centreline of a vortex tube of flux Φ_i. Each component γ_i is a disjoint component of $\mathcal{L}$ that does not intersect with any other γ_j, $i \neq j$. We have:

Theorem 1.2 ([30, 34]) *The total helicity of a vortex link $\mathcal{L}$ is given by*

$$H\left(\mathcal{L}\right) = H_{\text{mutual}} + H_{\text{self}} = \sum_{i\neq j}\Phi_i\Phi_j Lk\left(\gamma_i,\gamma_j\right) + \sum_{i=j}\Phi_i^2 Sl\left(\gamma_i\right)\,, \tag{1.4}$$

where H_{mutual} denotes the helicity contribution due to the mutual linking of γ_i and γ_j due to $Lk\left(\gamma_i,\gamma_j\right) \equiv Lk_{ij}$ (Gauss' linking number of γ_i and γ_j), while H_{self} is the self-linking contribution associated with γ_i due to $Sl\left(\gamma_i\right) \equiv Sl_i$ (self-linking of γ_i given by the Călugăreanu-White invariant).

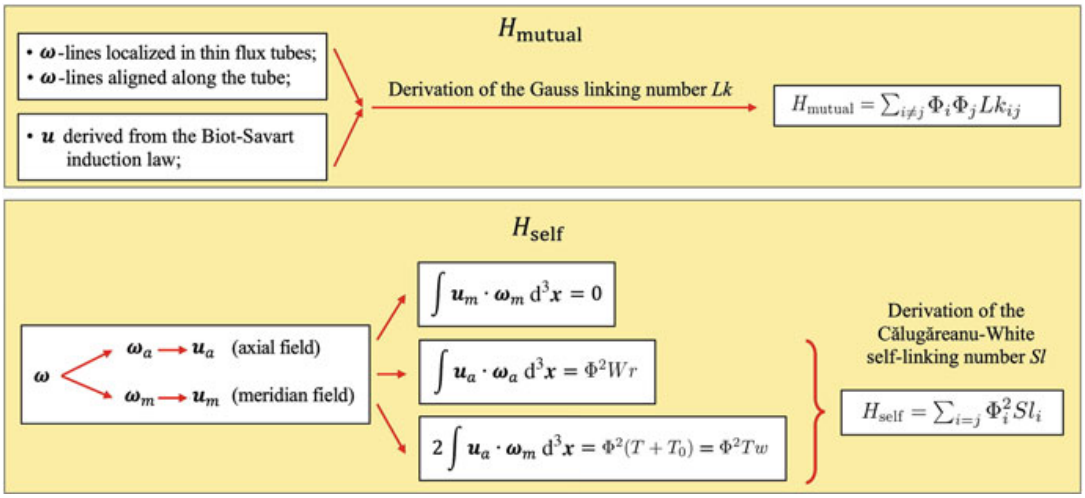

Fig. 1.1 Scheme of the proof of Theorem 1.2

A sketch of the proof is shown in Fig. 1.1 and details can be found in [30, 34, 43]. The Călugăreanu-White self-linking number is a topological invariant of a physical knot given by the fundamental formula [12, 53]:

$$Sl = Wr + Tw = Wr + T + T_0 \,, \tag{1.5}$$

where Wr denotes the writhing number, Tw the total twist number, and T and T_0 denote the normalised total torsion and the intrinsic twist of each component, all global geometric quantities of the physical knot. Evidently when $\Phi_1 = \cdots = \Phi_N = \Phi$, Eq. (1.4) takes the simpler form

$$H(\mathcal{L}) = H_{\text{mutual}} + H_{\text{self}} = \Phi^2 \left(\sum_{i\neq j} Lk(\gamma_i, \gamma_j) + \sum_{i=j} Sl(\gamma_i) \right). \tag{1.6}$$

Equation (1.4) transforms a computationally challenging volume integral to a directly computable algebraic expression in terms of topological and geometric quantities, a simplification of remarkable importance for both theoretical and practical applications. Indeed, mutual linking and writhing number can be measured by their algebraic interpretation in terms of signed crossings [46]. According to the sign convention of Fig. 1.2, we have

$$Lk(\gamma_i, \gamma_j) = \frac{1}{2} \sum_{r\in\{\gamma_i \sqcap \gamma_j\}} \varepsilon_r \,, \qquad Wr(\gamma_i) = \langle \sum_{r\in\{\gamma_i \sqcap \gamma_i\}} \varepsilon_r \rangle \,, \tag{1.7}$$

where $\{\gamma_i \sqcap \gamma_j\}$ and $\{\gamma_i \sqcap \gamma_i\}$ denote respectively the set of apparent intersections between γ_i and γ_j, and self-intersections of γ_i, present in the diagram projection of $\mathcal{L}$. The writhing number Wr is defined in terms of the space averaging (denoted by the angular brackets) over all possible viewing directions of γ_i. For an illustration

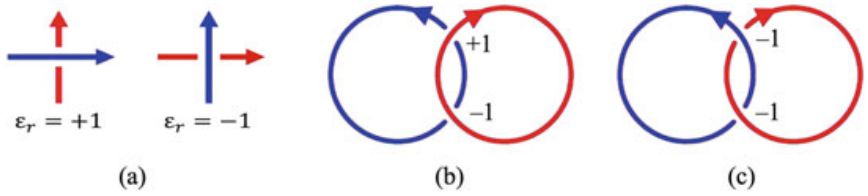

Fig. 1.2 (**a**) Algebraic sign associated with a crossing site: $\varepsilon_r = +1$, over-crossing; $\varepsilon_r = -1$, under-crossing. Indented diagrams of (**b**) the unlink, given by two unlinked, oriented rings with Gauss' linking number $Lk = 0$, and (**c**) the negative Hopf link with linking number $Lk = -1$

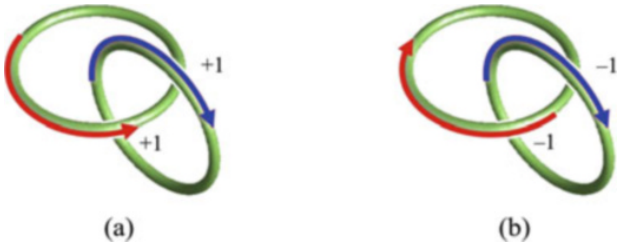

Fig. 1.3 Two different Hopf links: (**a**) positive Hopf link $\boldsymbol{H}_+$ ($Lk = +1$), and (**b**) negative Hopf link $\boldsymbol{H}_-$ ($Lk = -1$)

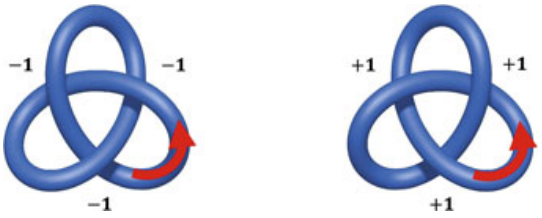

Fig. 1.4 Left-handed trefoil $\boldsymbol{T}^L$ of directional writhe $\tilde{W}r \approx -3$, and right-handed trefoil $\boldsymbol{T}^R$ of directional writhe $\tilde{W}r \approx +3$

of the direct computation of these values we can consider the elementary examples shown in Figs. 1.2 and 1.3. The unlink ($Lk = 0$), and the negative Hopf link ($Lk = -1$) are shown in Fig. 1.2. If we reverse one strand orientation, the crossing sign changes; by this operation we have the family of chiral knots and links, given by the mirror image of the original configuration. An example of this is shown by the positive and negative Hopf links of Fig. 1.3.

The exact value of the writhing number is given by the second equation of (1.7). Since the exact value is difficult to get in practice, an approximated value can be obtained by replacing the space averaging with the weighted algebraic summation of the signed crossing given, for example, by three mutually orthogonal projections of the knot centreline. This way we obtain an estimated value of the writhe ($Wr_\perp$), which provides a very good approximation of the exact value [5]. In the case of almost planar configurations we can consider the directional writhe ($\tilde{W}r$) computed from the single diagram obtained from the viewing projection along the direction normal to the planar configuration. Examples of directional writhe computations for the left-handed and right-handed trefoil knots are shown in Fig. 1.4.

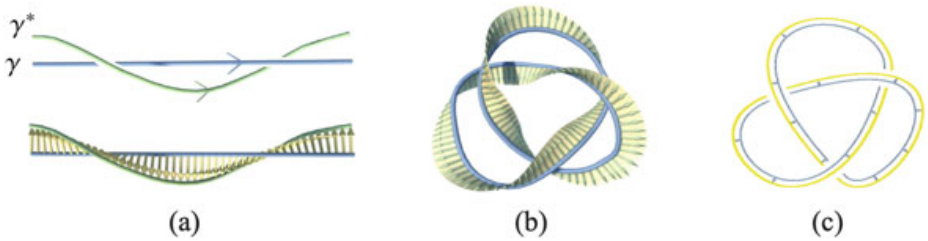

Fig. 1.5 (**a**) The straight line represents a knot centreline, and the curve γ^* around γ determines the mathematical ribbon; (**b**) a framed trefoil; (**c**) a blackboard framing of the trefoil knot (image adapted from [15])

The other two contributions left out from the computation of Sl are total torsion and intrinsic twist. Total torsion T is measured by the space geometry of the knot centreline γ_i; because it involves third derivatives of the arc-length, this contribution is generally rather modest. A numerical estimate based on torus knots shows [36] that T may account for a few percentages of the total self-linking number, so that for practical applications it can be ignored.

The intrinsic twist T_0 is in general very hard to compute. It is mathematically defined by the rotation of a mathematical ribbon $R = R(\gamma_i, \gamma_i^*)$ defined by the knot centreline γ_i and its pushoff curve γ_i^* (the other edge of the ribbon) in the non-zero section of the normal bundle of the knot (see Fig. 1.5). The ribbon provides a framing for the physical knot; the zero-framing condition is given by $Lk(\gamma_i, \gamma_i^*) = 0$; the field lines winding in the knotted flux tube is therefore measured with respect to this framing.

For physical applications we can use the simplified algebraic expression given by

$$H(\mathcal{L}) \approx \Phi^2 \left(\frac{1}{2} \sum_{r \in \{\gamma_i \sqcap \gamma_j\}} \varepsilon_r + \langle \sum_{r \in \{\gamma_i \sqcap \gamma_i\}} \varepsilon_r \rangle_\perp \right). \tag{1.8}$$

Alternatively, when fields can be measured directly by numerical simulations, we can extract total twist information from the combined use of the evaluation of the helicity integral and the crossing sign estimate. Hence, from (1.1) and (1.8), we have

$$Tw(\mathcal{L}) \approx \int_V \boldsymbol{u} \cdot \boldsymbol{\omega} \, \mathrm{d}^3\boldsymbol{x} - \Phi^2 \left(\frac{1}{2} \sum_{r \in \{\gamma_i \sqcap \gamma_j\}} \varepsilon_r + \langle \sum_{r \in \{\gamma_i \sqcap \gamma_i\}} \varepsilon_r \rangle_\perp \right). \tag{1.9}$$

Since during evolution flux tubes change topology through interaction and reconnection of knot strands, information on twist change across reconnections helps to estimate energy transfers between fluid knots.

1.2 Knot Polynomial Invariants and Helicity

Topological information based purely on crossing number and linking numbers is known to have flaws due to the limitation of detecting different link types. Typical examples are shown in Fig. 1.6, where the linking number fails to distinguish 3 unlinked circles from the Whitehead link, or the Borromean rings. Helicity computation based purely on linking numbers evidently suffers from this limitation. It is therefore important to look for more powerful topological information, and this is provided by knot polynomial invariants.

1.2.1 Helicity as an Abelian Chern-Simons Action

In order to introduce knot polynomials in topological fluid mechanics it is useful to re-consider helicity in a new setting. Here we present a concise review of the work done, based on a series of papers that the interested reader may consult for details [25, 26, 41].

In the language of exterior differential forms the velocity field $\boldsymbol{u}$ is a 1-form given by $u = u_i \mathrm{d}x^i$, and $\mathrm{d}u$ is thus a 2-form given by $\mathrm{d}u = \frac{1}{2}\partial_i u_j \mathrm{d}x^i \wedge \mathrm{d}x^j$, where $\wedge$ denotes the standard wedge product. The vorticity field $\boldsymbol{\omega}$ is also a 1-form defined by the Hodge dual $\omega = *\mathrm{d}u$, that is $\omega = \omega_i \, \mathrm{d}x^i = \left(\epsilon_i{}^{jk} \partial_j u_k\right) \mathrm{d}x^i$. The helicity integral (1.1) can thus be written as a 3-form, given by

$$H = \int_V u \wedge \mathrm{d}u \; ; \tag{1.10}$$

the above integral can be interpreted as an Abelian Chern-Simons (CS) action. Generally speaking, a CS action S_{CS} with a generic, non-Abelian group G, is given [3] by

$$S_{CS} = \frac{k}{4\pi} \int_{\mathcal{M}} CS(A) = \frac{k}{4\pi} \int_{\mathcal{M}} \left(A \wedge dA + \frac{2}{3} A \wedge A \wedge A \right) ; \tag{1.11}$$

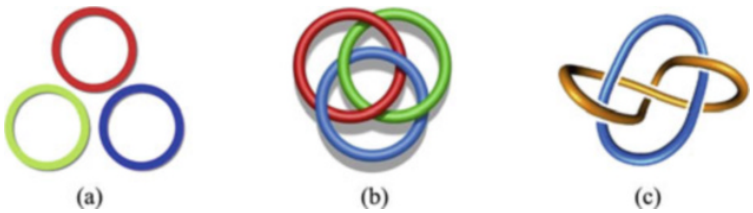

Fig. 1.6 (**a**) 3 unlinked circles, (**b**) the Borromean rings, (**c**) the Whitehead link; regardless of their relative orientation, these different topological configurations share the same linking number $Lk = 0$

here $k/4\pi \in \mathbb{R}$ is a (level) parameter, $CS(A)$ is the so-called CS 3-form, $A = A(x)$ is a connection 1-form on the principal-G bundle (i.e. a gauge potential) given by $A = A_i^a T_a \mathrm{d}x^i$, $\{T_a\}$ $(a = 1, \cdots, \dim(G))$ the generators of G, and $\{x^i\}$ $(i = 1, 2, 3)$ the set of coordinates of the 3-dimensional base manifold $\mathcal{M}$. When G is non-Abelian (the generic case) $[T_a, T_b] \neq 0$, thus the cubic term $A \wedge A \wedge A$ does not vanish. In the special case of $G = U(1)$ (Abelian group) the cubic term vanishes, so that we have

$$S_{CS} = \frac{k}{4\pi} \int_V A \wedge \mathrm{d}A \,. \tag{1.12}$$

By direct comparison of (1.10) with (1.12), since the velocity field u can be regarded as a gauge potential (cf. the London relation in superconductivity [14]), we can interpret the fluid helicity (1.10) as a special Abelian case of the CS action (1.11) (setting $k/4\pi = 1$).

Following the revolutionary work of Witten [54], CS theory has become the benchmark of a topological quantum field theory (TQFT). Witten showed that the non-local, physical observables of the CS theory (called Wilson loops), can be represented by knots in a 3-dimensional spacetime, and can be computed by knot polynomial invariants that generalize the celebrated Jones polynomial [17]. A physical interpretation of these invariants comes from the TQFT description of the CS path integrals. These are defined as the vacuum expectation value of the Wilson loops, according to the expression

$$\left\langle \prod_i \mathrm{e}^{\mathrm{i} \oint_{\gamma_i} A} \right\rangle = \frac{1}{Z} \int [\mathcal{D}A] \left(\mathrm{e}^{\mathrm{i} \sum_i \oint_{\gamma_i} A} \right) \mathrm{e}^{\mathrm{i} 2\pi S_{CS}} \,. \tag{1.13}$$

Wilson loops are gauge invariant operators that arise from the parallel transport of gauge variables around closed loops γ_i, and are represented by the expression $\exp\left(\mathrm{i} \sum_i \oint_{\gamma_i} A\right)$. The term $[\mathcal{D}A]$ represents a functional integration performed on A, where Z is a partition function that plays the role of a normalisation constant. As usual γ_i denotes the i-th component of the link $\mathcal{L}$. Replacing the potential A with the velocity u, and the CS action with the helicity, the integrand becomes

$$\mathrm{e}^{\mathrm{i} \sum_i \oint_{\gamma_i} u} \mathrm{e}^{\mathrm{i} \int_V u \wedge \mathrm{d}u} = \mathrm{e}^{\mathrm{i} \sum_i \oint_{\gamma_i} u} \mathrm{e}^{\mathrm{i} H} \,. \tag{1.14}$$

Now, let us turn our attention to the vorticity localised into thin flux tubes; by taking $\boldsymbol{\omega} = \omega_0 \hat{\boldsymbol{t}}$, with ω_0 constant, and $\hat{\boldsymbol{t}}$ unit tangent to γ_i, we can replace the helicity integral (1.1) with the field line helicity [5, 7, 47], given by

$$H = \sum_i \Phi_i \oint_{\gamma_i} \boldsymbol{u} \cdot \mathrm{d}\boldsymbol{x} \,, \tag{1.15}$$

where Φ is the flux associated with ω_0. H is thus reduced to a sum of line integrals along γ_i; taking for simplicity $\Phi_i = \Phi = 1$ $(i = 1, \ldots, N)$, we have

$$H = \sum_i \oint_{\gamma_i} u \,, \tag{1.16}$$

where u is the Biot-Savart velocity 1-form. By substituting this line integral into (1.14), we have

$$\mathrm{e}^{\mathrm{i}\sum_i \oint_{\gamma_i} u} \mathrm{e}^{\mathrm{i}H} = \left(\mathrm{e}^{\mathrm{i}H}\right)^2 . \tag{1.17}$$

where the key ingredient $e^{\mathrm{i}H}$ is expressed in terms of the field line helicity (1.16). This means that in the classical approach, one can drop the path integral formalism, and construct the knot polynomials as physical observables from the operator $e^{\mathrm{i}H}$.

1.2.2 Knot Polynomial Invariants in Classical Knot Theory

Let us briefly review some basic aspects of knot theory to introduce knot polynomials (for details see, for instance, [18]). A mathematical knot is simply a smooth embedding of a closed, non-self-intersecting, space curve γ, defined by the mapping $\gamma : S^1 \to \mathbb{R}^3$. Since a knotted flux tube is a tubular knot endowed with thickness, a way to relate physical knots to mathematical knots is to consider framed knots. A central aspect of knot theory is to establish the topological equivalence of two given knots (or links) under continuous deformation by the existence of isotopy invariants (such as linking numbers). An elementary technique to establish topological equivalence of two given knots is based on performing Reidemeister moves (denoted by R1, R2, R3 in Fig. 1.7) on the knot strands, so as to reduce two different knot projections to the same configuration. We have

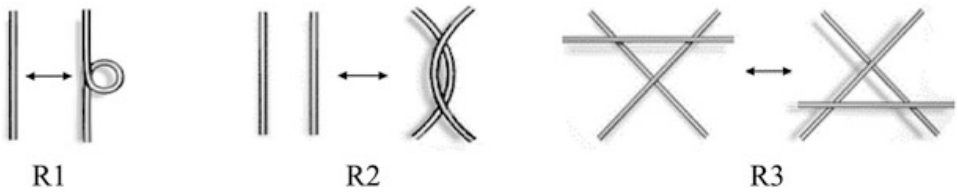

Fig. 1.7 The three Reidemeister moves R1, R2 and R3 performed on knot strands (thickened for visualization purposes). Two knots/links are topologically equivalent under ambient isotopy defined by performing the three Reidemeister moves. Regular isotopy is defined by equivalence under moves R2 and R3

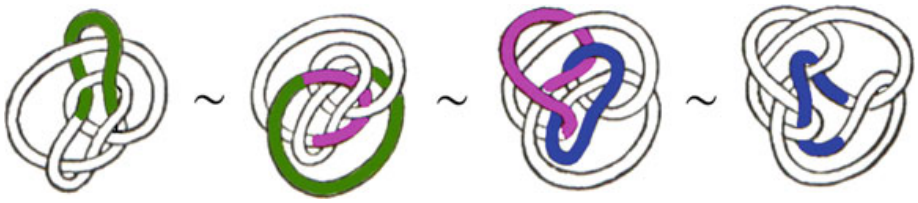

Fig. 1.8 Iterated application of the Reidemeister moves on coloured strands deforms the knot on the left to the knot on the right (and vice-versa). This proves that the knot on the far left and that on the far right (known as Perko pair) are actually the same knot type

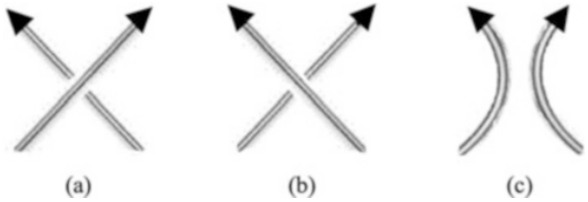

Fig. 1.9 By switching (**a**) an over-crossing of the diagram D_+, we obtain (**b**) an under-crossing (diagram D_-); the state (**c**) is obtained by performing an orientation-preserving "smoothing" of the same crossing (thus obtaining the diagram D_0)

Theorem 1.3 ([39]) *Two knots (or links) are topologically equivalent if and only if one can be transformed into the other by performing a finite sequence of Reidemeister moves of type R1, R2 and R3.*

A remarkable example of this is shown in Fig. 1.8.

Let us consider the indented diagram projection of an oriented knot, where the orientation is naturally induced by the constituent vector field lines of the physical knot; let us focus on the occurrence of the three states identified by an apparent over-pass, under-pass and presence of two parallel strands, as shown in Fig. 1.9. A change of state is a virtual operation performed on a knot diagram by selecting one particular state. A knot polynomial is determined by considering the following steps:

(i) given a generic projected knot diagram select an apparent crossing site (say an over-crossing): call this diagram D_+ ;
(ii) switch the selected crossing to its counterpart (an under-crossing) to obtain a second, different diagram D_-;
(iii) smooth-out the selected crossing by conserving the strand orientation so to get a third, different diagram D_0.

By analysing these 3 diagrams a knot polynomial is constructed by implementing its defining skein relation [19]. Let $\boldsymbol{U}_1$ denote the oriented unknot ◯ . We have [17]:

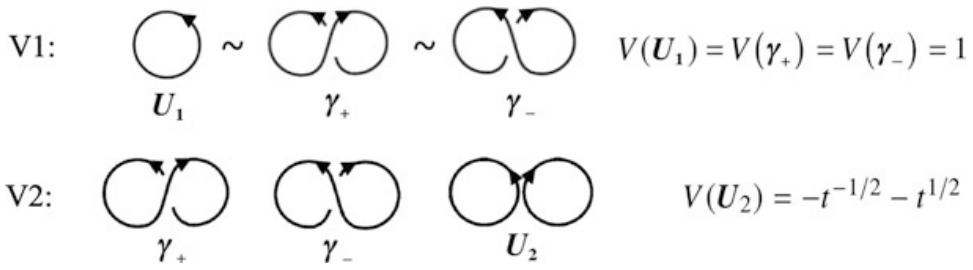

Fig. 1.10 Example of computation of the Jones polynomial of two unknotted, unlinked circles $\boldsymbol{U}_2$: (i) apply the relation V1 to the unknotted loop $\boldsymbol{U}_1$, with $V(\boldsymbol{\gamma}_+) = V(\boldsymbol{\gamma}_-) = 1$; (ii) apply the relation V2 to $\boldsymbol{\gamma}_+$ by switching the apparent crossing from positive to negative, and smoothing it, so to get $V(\boldsymbol{U}_2)$ (image adapted from [25])

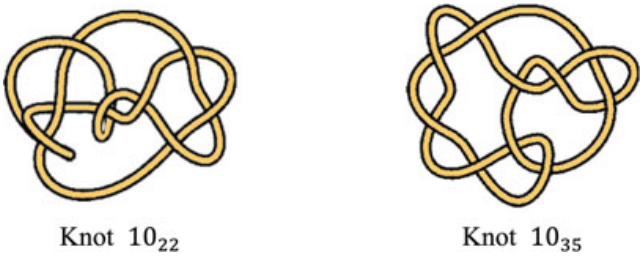

Fig. 1.11 The knots 10_{22} and 10_{35} have 10 minimal crossings, but they are different knot types, i.e. one cannot be isotoped to the other by continuous deformations. They share the same Jones polynomial, but they have different HOMFLYPT polynomials

Definition 1.1 Let $\mathcal{L}$ be an oriented knot/link type. The *Jones polynomial* $V_{\mathcal{L}}(t) = V(t)$ in the single dummy variable t is defined by the following relations:

$$\text{V1}: \quad V(\boldsymbol{U}_1) = 1 \,, \tag{1.18}$$

$$\text{V2}: \quad t^{-1}V(D_+) - tV(D_-) = (t^{1/2} - t^{-1/2})V(D_0) \,. \tag{1.19}$$

In order to have an idea on how these relations can be applied to get a polynomial invariant, consider the elementary example of Fig. 1.10: the polynomial $V(\boldsymbol{U}_2)$ of two unknotted, unlinked loops $\boldsymbol{U}_2$ is computed by considering the diagram D_+ of a positively coiled unknot $\boldsymbol{\gamma}_+$.

Similarly to linking numbers, knot polynomials have also limitations (see the example of Fig. 1.11); this stimulated the search for further improvements. A more elaborate polynomial is given by the HOMFLYPT polynomial [16, 38]:

Definition 1.2 Let $\mathcal{L}$ be an oriented knot/link type. The *HOMFLYPT polynomial* $P_{\mathcal{L}}(a, z) = P(a, z)$ in the two dummy variables a and z is defined by the following skein relation:

$$\text{P1}: \quad P(\boldsymbol{U}_1) = 1 \,, \tag{1.20}$$

$$\text{P2}: \quad aP(D_+) - a^{-1}P(D_-) = zP(D_0) \,. \tag{1.21}$$

HOMFLYPT can be thought of as a generalised version of the Jones polynomial, since $P(\mathcal{L})$ reduces to $V(\mathcal{L})$ by taking

$$a = t^{-1}\,, \qquad z = a^{-1/2} - a^{1/2} = t^{1/2} - t^{-1/2}\,. \tag{1.22}$$

We have

Theorem 1.4 ([16, 38]) *Let $\mathcal{L}$ and $\mathcal{L}'$ be two ambient isotopic, oriented knot/link types. The HOMFLYPT polynomial $P(\mathcal{L})$ is an isotopy invariant of $\mathcal{L}$, and $P(\mathcal{L}) = P(\mathcal{L}')$.*

Evidently the same holds true for $V(\mathcal{L})$. Now, since the mirror image of a given knot is not isotopic to the original knot (see, for instance, the two trefoils of Fig. 1.4), let's see how $P(\mathcal{L})$ is related to the polynomial of its mirror image $\tilde{\mathcal{L}}$.

Lemma 1.1 *Let $P(\mathcal{L})$ be the HOMFLYPT polynomial of the link $\mathcal{L}$, and $P(\tilde{\mathcal{L}})$ the corresponding polynomial of its mirror image $\tilde{\mathcal{L}}$. By taking*

$$\tilde{a} = a^{-1}\,, \qquad \tilde{z} = -z\,, \tag{1.23}$$

$P(\mathcal{L})$ reduces to $P(\tilde{\mathcal{L}})$ in the new variables $\tilde{a}$, $\tilde{z}$.

Proof From the skein relation P2, we have

$$a\,P(\mathcal{L}_+) - a^{-1}\,P(\mathcal{L}_-) = z\,P(\mathcal{L}_0)\,. \tag{1.24}$$

By the mirror transformation, we have

$$\mathcal{L}_+ \longrightarrow \tilde{\mathcal{L}}_-\,, \qquad \mathcal{L}_- \longrightarrow \tilde{\mathcal{L}}_+\,, \qquad \mathcal{L}_0 \longrightarrow \tilde{\mathcal{L}}_0\,, \tag{1.25}$$

where $\mathcal{L}_-$ and $\mathcal{L}_0$ denote the link diagrams obtained by switching and smoothing a crossing site of the diagram $\mathcal{L}_+$. By direct application of (1.25) and substitution of (1.23) we can reduce (1.24) to the P2 of $\tilde{\mathcal{L}}$, given by

$$\tilde{a}\,P(\tilde{\mathcal{L}}_+) - \tilde{a}^{-1}\,P(\tilde{\mathcal{L}}_-) = \tilde{z}\,P(\tilde{\mathcal{L}}_0)\,, \tag{1.26}$$

as stated. □

Similarly, for the Jones polynomial:

Corollary 1.1 *Let $V(\mathcal{L})$ be the Jones polynomial of the link $\mathcal{L}$, and $V(\tilde{\mathcal{L}})$ the corresponding polynomial of its mirror image $\tilde{\mathcal{L}}$. By taking*

$$\tilde{t} = t^{-1}\,, \tag{1.27}$$

$V(\mathcal{L})$ reduces to $V(\tilde{\mathcal{L}})$ in the parameter $\tilde{t}$.

For applications it is useful to recall the following properties. Let $\mathcal{L}_1 \# \mathcal{L}_2$ denote the connected sum of two oriented links $\mathcal{L}_1$ and $\mathcal{L}_2$, and $\mathcal{L}_1 \sqcup \mathcal{L}_2$ their disjoint union. Assuming that $\mathcal{L}_1$ and $\mathcal{L}_2$ are well separated, so that no part of $\mathcal{L}_1$ crosses over or under any part of $\mathcal{L}_2$, we have:

Lemma 1.2 ([24]) *Given two oriented links $\mathcal{L}_1$ and $\mathcal{L}_2$, we have*

$$\text{(i)} \quad \mathrm{P}(\mathcal{L}_1 \# \mathcal{L}_2) = \mathrm{P}(\mathcal{L}_1)\mathrm{P}(\mathcal{L}_2) \; ; \tag{1.28}$$

$$\text{(ii)} \quad \mathrm{P}(\mathcal{L}_1 \sqcup \mathcal{L}_2) = \delta \mathrm{P}(\mathcal{L}_1)\mathrm{P}(\mathcal{L}_2) \; , \tag{1.29}$$

where $\delta = (a - a^{-1})/z$.

1.2.2.1 Examples of Polynomial Computation for the Hopf Link and the Trefoil Knot

Here we show how to derive the HOMFLYPT and Jones polynomials for the Hopf link and the trefoil knot by direct application of the polynomial skein relation.
Positive Hopf link $\boldsymbol{H}_+$. Let's apply P2 considering the positive crossing site of $\boldsymbol{H}_+$ and the reduction scheme of Fig. 1.12. Equation (1.21) becomes

$$a P\left(\boldsymbol{H}_+\right) - a^{-1} P(\boldsymbol{U}_2) = z P(\boldsymbol{U}_1) \; , \tag{1.30}$$

i.e.

$$P\left(\boldsymbol{H}_+\right) = a^{-2} P(\boldsymbol{U}_2) + a^{-1} z P(\boldsymbol{U}_1) = a^{-2}\delta + a^{-1} z \; , \tag{1.31}$$

thus giving the HOMFLYPT polynomial of $\boldsymbol{H}_+$, that is

$$P\left(\boldsymbol{H}_+\right) = -a^{-3} z^{-1} + a^{-1} z^{-1} + a^{-1} z \; . \tag{1.32}$$

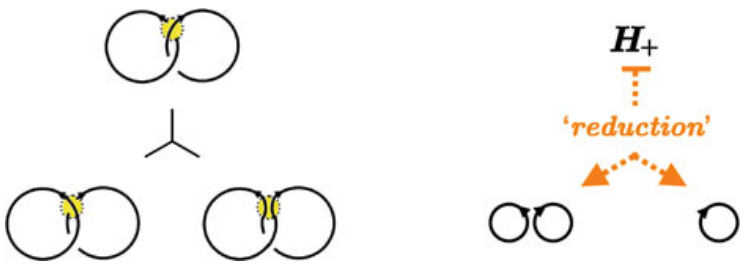

Fig. 1.12 Diagrammatic interpretation of the skein relation (1.21) as a reduction scheme: application of P2 to the positive crossing of the Hopf link $\boldsymbol{H}_+$ (image adapted from [26])

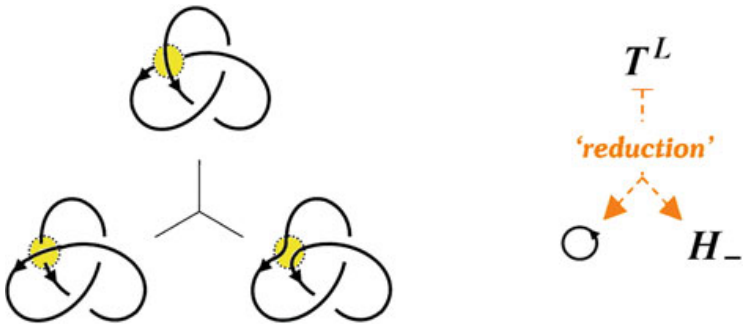

Fig. 1.13 Diagrammatic interpretation of the skein relation (1.21) as a reduction scheme: application of P2 to the negative crossing of the left-handed trefoil $\boldsymbol{T}^L$

Using (1.22), we obtain the Jones polynomial of $\boldsymbol{H}_+$:

$$V\,(\boldsymbol{H}_+) = -t^{\frac{1}{2}} - t^{\frac{5}{2}}\,. \tag{1.33}$$

Negative Hopf link $\boldsymbol{H}_-$. This is the mirror image of $\boldsymbol{H}_+$; using Lemma 1.1 the HOMFLYPT polynomial becomes

$$P\,(\boldsymbol{H}_-) = a^3 z^{-1} - a z^{-1} - a z\,, \tag{1.34}$$

and by Eq. (1.22) we have the Jones polynomial

$$V\,(\boldsymbol{H}_-) = -t^{-\frac{1}{2}} - t^{-\frac{5}{2}}\,. \tag{1.35}$$

Left-Handed Trefoil $\boldsymbol{T}^L$ According to the scheme of Fig. 1.13, we have

$$a\,P(\boldsymbol{U}_1) - a^{-1} P(\boldsymbol{T}^L) = z P\,(\boldsymbol{H}_-)\,, \tag{1.36}$$

that is

$$P(\boldsymbol{T}^L) = a^2 P(\boldsymbol{U}_1) - a z P(\boldsymbol{H}_-) = a^2 - a z(a^3 z^{-1} - a z^{-1} - a z)\,; \tag{1.37}$$

hence, the HOMFLYPT polynomial reads

$$P(\boldsymbol{T}^L) = 2a^2 + a^2 z^2 - a^4\,, \tag{1.38}$$

and the Jones polynomial is given by

$$V(\boldsymbol{T}^L) = -t^{-4} + t^{-3} + t^{-1}\,. \tag{1.39}$$

	Jones polynomial	HOMFLYPT polynomial
$\boldsymbol{U}_N$	$\delta^{N-1} = (-t^{1/2} - t^{-1/2})^{N-1}$	$\delta^{N-1} = [(a - a^{-1})/z]^{N-1}$
$\mathcal{L} \sqcup \boldsymbol{U}_1$	$V(\mathcal{L})\,\delta$	$P(\mathcal{L})\,\delta$
$\boldsymbol{H}_+$	$-t^{1/2} - t^{5/2}$	$a^{-1}z + (a^{-1} - a^{-3})\,z^{-1}$
$\boldsymbol{H}_-$	$-t^{-1/2} - t^{-5/2}$	$-az - (a - a^3)\,z^{-1}$
$\boldsymbol{T}^L$	$-t^{-4} + t^{-3} + t^{-1}$	$2a^2 + a^2z^2 - a^4$
$\boldsymbol{T}^R$	$-t^4 + t^3 + t$	$2a^{-2} + a^{-2}z^2 - a^{-4}$
$\boldsymbol{F}^8$	$t^{-2} - t^{-1} + 1 - t + t^2$	$a^{-2} - 1 - z^2 + a^2$
$\boldsymbol{W}$	$t^{-7/2} - 2t^{-5/2} + t^{-3/2} - 2t^{-1/2} + t^{1/2} - t^{3/2}$	$-a^{-1}z^{-1} - a^{-1}z + az^{-1} + 2az + az^3 - a^3z$
$\tilde{\boldsymbol{W}}$	$t^{7/2} - 2t^{5/2} + t^{3/2} - 2t^{1/2} + t^{-1/2} - t^{-3/2}$	$az^{-1} + az - a^{-1}z^{-1} - 2a^{-1}z - a^{-1}z^3 + a^{-3}z$
$\boldsymbol{B}$	$-t^{-3} + 3t^{-2} - 2t^{-1} + 4 - 2t + 3t^2 - t^3$	$a^{-2}z^{-2} - a^{-2}z^2 + a^2z^{-2} - a^2z^2 - 2z^{-2} + 2z^2 + z^4$

Fig. 1.14 Jones and HOMFLYPT polynomials of some elementary oriented knots and links

Right-Handed Trefoil $\boldsymbol{T}^R$ This is the mirror image of $\boldsymbol{T}^L$; the HOMFLYPT polynomial of $\boldsymbol{T}^R$ is given by

$$P(\boldsymbol{T}^R) = 2a^{-2} + a^{-2}z^2 - a^{-4}\,, \tag{1.40}$$

and the Jones polynomial is given by

$$V(\boldsymbol{T}^R) = -t^4 + t^3 + t\,. \tag{1.41}$$

The table of Fig. 1.14 shows the Jones and HOMFLYPT polynomials of the following knot and link types: N unknots $\boldsymbol{U}_N$, disjoint union of a link and an unknot $\mathcal{L} \sqcup \boldsymbol{U}_1$, positive and negative Hopf link $\boldsymbol{H}_+$ and $\boldsymbol{H}_-$, left- and right-handed trefoil knot $\boldsymbol{T}^L$ and $\boldsymbol{T}^R$, figure-of-eight knot $\boldsymbol{F}^8$, Whitehead link $\boldsymbol{W}$ and mirror image $\tilde{\boldsymbol{W}}$, Borromean rings $\boldsymbol{B}$.

1.2.3 Derivation of the Adapted Jones Polynomial from Helicity

Using the skein relation of the Jones polynomial we can prove the following result:

Theorem 1.5 ([25]) *Let $H = H(\mathcal{L})$ be the helicity of a physical framed knot/link $\mathcal{L}$. Then*

$$\mathrm{e}^{H(\mathcal{L})} = \mathrm{e}^{\oint_{\mathcal{L}} \boldsymbol{u}\cdot \mathrm{d}\boldsymbol{x}}\,, \tag{1.42}$$

appropriately re-scaled, satisfies (with a plausible statistical hypothesis) the skein relation of the Jones polynomial $V = V(\mathcal{L})$.

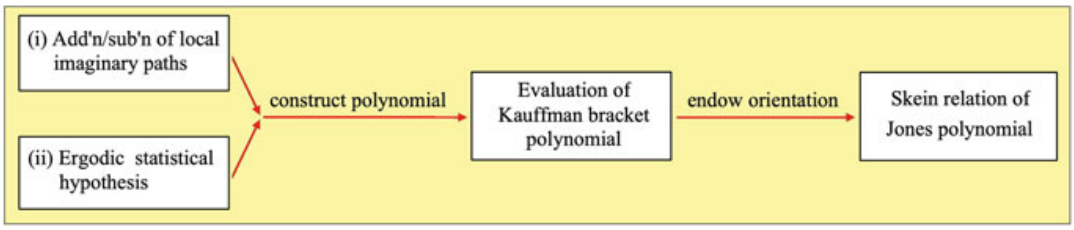

Fig. 1.15 Scheme of the proof of Theorem 1.5

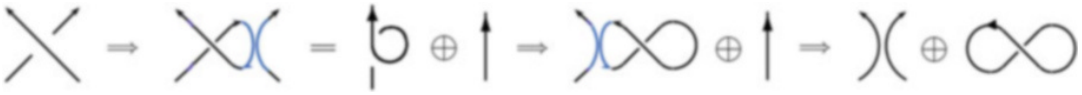

Fig. 1.16 Crossing state decomposition by addition and subtraction of "imaginary paths"; note the interpretation of the crossing state in terms of the closed curl (image adapted from [26])

For details of the proof see [25, 41]. The derivation is outlined in Fig. 1.15, where we make two assumptions: (i) since vortex knots are naturally led to interact and reconnect locally, in analogy with the theory of particle interactions we assume that reconnection events can be described by a virtual operation of addition and subtraction of vortex strands (interpreted mathematically as "imaginary paths"), according to the scheme of Fig. 1.16. (ii) We also assume (statistical hypothesis) that the two decompositions above have equal probability to occur.

For physical applications we can relate the Jones single variable t with the helicity $H(\mathcal{L})$; considering zero-framed knots, writhe and twist are interlocked by the zero helicity condition (as for vortex defects in condensed matter physics [6, 51]), i.e. $Sl = Wr + Tw = 0$. By identifying (say) writhe with the t variable, we can take for example

$$t^{1/2} = \mathrm{e}^{H} = \mathrm{e}^{\lambda_\omega Wr} \,, \tag{1.43}$$

where $\lambda_\omega \in [0, 1]$ represents the uncertainty associated with the directional writhe. From direct measurements, or estimates, of the average writhe $\langle Wr \rangle$, we can then associate a numerical value to the topology of fluid knots, given by the adapted Jones polynomial.

1.2.4 Derivation of the Adapted HOMFLYPT Polynomial from Helicity

Following a similar strategy we can extend this approach to derive from the helicity $H(\mathcal{L})$ the 2-variable HOMFLYPT polynomial $P(\mathcal{L}) = P(\mathcal{L}; a, z)$ in the parameters a and z. We have

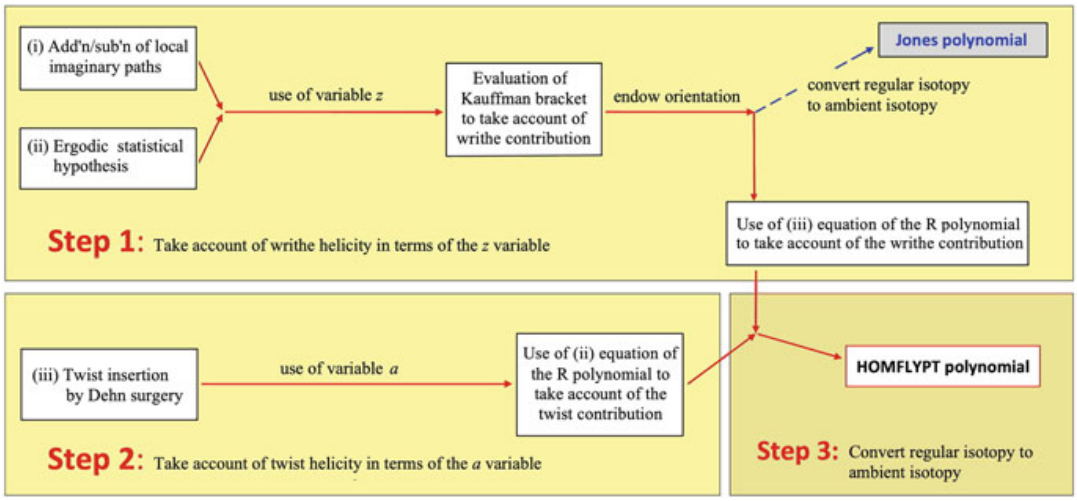

Fig. 1.17 Scheme of the proof of Theorem 1.6

Theorem 1.6 ([26]) *Let $H = H(\mathcal{L})$ be the helicity of a physical framed knot/link $\mathcal{L}$. Then*

$$\mathrm{e}^{H(\mathcal{L})} = \mathrm{e}^{\oint_{\mathcal{L}} \boldsymbol{u}\cdot \mathrm{d}\boldsymbol{x}}\,, \tag{1.44}$$

appropriately re-scaled, satisfies (with a plausible statistical hypothesis) the skein relation of the HOMFLYPT polynomial $P = P(\mathcal{L})$.

The derivation in this case is more elaborate as shown by the two distinct paths denoted by Step 1 and Step 2 of Fig. 1.17. We first observe that the regular isotopy version of the HOMFLYPT polynomial (the so-called *R-polynomial*) is given by the following relations [18]:

$$\text{(i)}: \quad R(\bigcirc) = 1\,, \tag{1.45}$$

$$\text{(ii)}: \quad R(\;\text{⌐}\!\!\supset) = aR(\uparrow)\,, \qquad R(\subset\!\!\text{⌐}) = a^{-1}R(\uparrow)\,, \tag{1.46}$$

$$\text{(iii)}: \quad R(\times) - R(\times) = zR(\;)(\;)\,, \tag{1.47}$$

where $\;\text{⌐}\!\!\supset\;$ denotes the Reidemeister twist move. By applying (1.47) to the Eq. (1.46), we have

$$R\left(\;\text{⌐}\!\!\supset\;\right) - R\left(\subset\!\!\text{⌐}\right) = aR\,(\uparrow) - a^{-1}R\,(\uparrow) = zR\,(\uparrow\bigcirc)\,, \tag{1.48}$$

that is

$$\delta R\left(\ \uparrow\ \right) = R\left(\uparrow\ \circlearrowright\right)\ , \tag{1.49}$$

where (as usual) $\delta = (a - a^{-1})/z$. By extending this equation to the knot diagram D, we get (Lemma 1.2)

$$R\left(D\ \circlearrowright\right) = \delta R\left(D\right)\ , \tag{1.50}$$

which can be considered a supplementary rule for the derivation of the knot polynomial. The regular isotopy version of the HOMFLYPT with variables z and a specialises to a regular isotopy version of the Jones polynomial when $z = a - a^{-1}$. We make the physical heuristic assumption that the variables a and z are independent of one another. Then these relations become relations for the HOMFLYPT polynomial, and this second stage is accomplished. For further details on these constructions see [26].

The physical interpretation of the two variables is accomplished by taking $z = k - k^{-1}$, so that

$$k = \mathrm{e}^{2\lambda_\omega Wr}\ , \qquad a = \mathrm{e}^{\lambda_\tau Tw}\ , \tag{1.51}$$

where $\lambda_\tau \in [0, 1]$ represents the uncertainty associated with twist; note that in our heuristics λ_ω and λ_τ are also assumed to be totally independent from one another. Since reduction to Jones implies $ak^2 = 1$, from (1.51) we have

$$\lambda_\tau Tw = -2\,(2\lambda_\omega Wr) = -4\lambda_\omega Wr\ , \tag{1.52}$$

that gives a relation between writhe and twist, i.e. $Wr = -(\lambda_\tau/4\lambda_\omega)Tw$. As we did for the Jones polynomial, the adapted HOMFLYPT can now be computed by the numerical values obtained from $\langle Wr\rangle$ and $\langle Tw\rangle$, so that we can quantify the topology of physical knots and links by numerical values. For example, if we take the average values $\langle\lambda_\omega\rangle = \langle Wr\rangle = 1/2$, and $\langle\lambda_\tau\rangle = \langle Tw\rangle = 1/2$, we obtain

$$z = \mathrm{e}^{1/2} - \mathrm{e}^{-1/2} \approx 1.04\ , \qquad a = \mathrm{e}^{1/4} \approx 1.28\ . \tag{1.53}$$

For prescribed values of a and z (given, for example, by Eq. (1.53)) we obtain numerical values for the adapted Jones and HOMFLYPT polynomials [42].

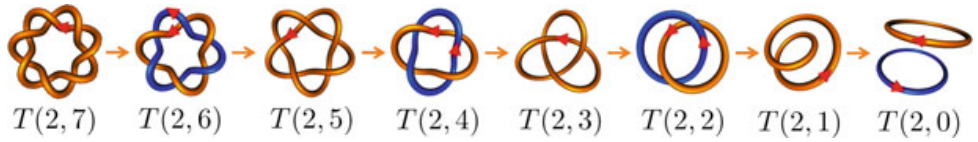

Fig. 1.18 Time sequence of topological transitions of torus knots and links due to a single reconnection event, starting from the torus knot $T(2,7)$ (image adapted from [27])

1.2.5 *Cascade of Torus Knots and Links in Terms of Adapted Polynomial Values*

Generic patterns of vortex torus knot evolution in water [20, 21] and DNA catenane unlinking [49, 50] show a surprising and remarkable similarity in the process of topological simplification. The change of topology, due to successive, orientation preserving reconnections induced by local physical mechanisms, generates a time-dependent pattern that can be exemplified by the topological cascade of torus knots and links $\{T(2,n)\}$ ($n \in \mathbb{N}$) shown in Fig. 1.18. Relying on the information provided by experiments, we can apply the theory of Sect. 1.2.4 to compute the numerical values of the adapted HOMFLYPT polynomial $P_{T(2,n)} = P[T(2,n)]$ in relation to the observed process. Since the family of torus knots and links admits representation in closed braid form, assuming continuous reduction of topological complexity in a stepwise manner we can apply the HOMFLYPT skein relations in a recursive way.

Theorem 1.7 ([27]) *Let us consider the family* $\{T(2,n)\}$ *of torus knots and links. The HOMFLYPT polynomial of* $T(2,n)$ *is given by*

$$P_{T(2,n)} = \left[\frac{k^{n-2} - (-k)^{-(n-2)}}{a^{n-3}\left(k + k^{-1}\right)}\right] P_{T(2,3)} + \left[\frac{k^{n-3} - (-k)^{-(n-3)}}{a^{n-3}\left(k + k^{-1}\right)}\right] P_{T(2,2)} \,, \tag{1.54}$$

where

$$P_{T(2,3)} = 2a^{-2} + a^{-2}z^2 - a^{-4} \,, \qquad P_{T(2,2)} = a^{-1}z + \left(a^{-1} - a^{-3}\right)z^{-1} \,. \tag{1.55}$$

For details of the derivation see [27]. By taking values compatible with the actual observations, we set

$$a = e^{\frac{1}{4}} \approx 1.28 \,, \qquad k = e^{\frac{1}{2}} \approx 1.65 \,, \quad z = k - k^{-1} \approx 1.04 \,. \tag{1.56}$$

Using these values, the adapted polynomials for $\{T(2,n)\}$ ($n = 0, 1, 2, \ldots, 10$) provide numerical estimates of topological complexity: the results are shown in Fig. 1.19. The obtained values form a monotonic decreasing sequence that appears to be consistent with the observed physical and topological cascade associated with the evolution, being also in good agreement with the expected energy decrease. This

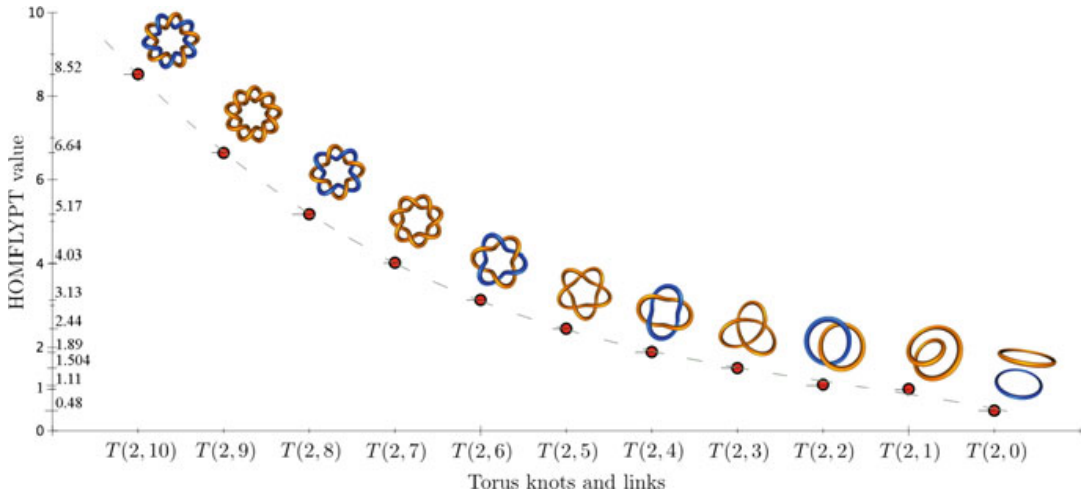

Fig. 1.19 Numerical values of the HOMFLYPT adapted polynomial computed for the set of torus knots/links $\{T(2,n)\}$ ($n = 0, 1, 2, \ldots, 10$), plotted against decreasing complexity (image adapted from [27])

correspondence can be justified as follows: on the one hand a topological change is due to a reconnection event, on the other hand since the energy of thin knots is essentially a linear function of length, any reconnection occurs at the expense of a small, but non-zero erosion of the knot length. There is therefore a direct relation between the topological simplification measured by the adapted polynomial and the expected energy decrease in the knot evolution. As we shall see in Sect. 1.3 below, by relying on simulation data of tight knots and links such a relationship has been established analytically for minimal energy states of magnetic knots [44], and a similar result has been proven also for a family of torus knots [36].

1.3 Groundstate Energy Spectra of Magnetic Knots and Links

An alternative way to explore the relation between topological complexity and energy is to consider steady state configurations of knots and links. Under steady conditions there is a perfect analogy between the Euler solutions for vortex knots and links, and topologically equivalent magnetic configurations. Since energy is a scalar quantity, it is natural to search for a scalar measure of topological complexity, and look for a correspondence between minimum energy levels of magnetic knots and topology.

Let us consider magnetic knots and links embedded in a perfectly conducting, incompressible fluid in $\mathbb{R}^3$, and subject to the ideal process of magnetic relaxation [31]. Magnetic knots are tubular embeddings of the magnetic field $\boldsymbol{B} = \boldsymbol{B}(\boldsymbol{x}, t)$ (where as usual $\boldsymbol{x}$ and t denote the vector position and time). The field is defined on nested tori that are centred in the tubular knot of axis γ and total length L; we

assume no-flux condition on each toroidal surface, including the tubular boundary that is a magnetic surface. For simplicity we take the tube cross-section to be circular, of radius R and area $A = \pi R^2$, so that the volume of the tubular knot is given by $V = \pi R^2 L$. Consider the class of magnetic fields of finite energy, given by

$$\boldsymbol{B} \in \left\{ \nabla \cdot \boldsymbol{B} = 0,\ \partial_t \boldsymbol{B} = \nabla \times (\boldsymbol{u} \times \boldsymbol{B}),\ L_2\text{−norm} \right\}, \tag{1.57}$$

transported by a fluid velocity $\boldsymbol{u} = \boldsymbol{u}(\boldsymbol{x}, t)$, such that $\nabla \cdot \boldsymbol{u} = 0$ everywhere, with $\boldsymbol{u} = 0$ at infinity. Under these conditions, volume, flux and knot type are conserved under the diffeomorphisms induced by the flow map induced by $\boldsymbol{u}$. To leading order the Lorentz force associated with $\boldsymbol{B}$ is proportional to the field lines curvature, so that under the action of this force the knot is gradually led to shrink, shortening its length; under volume conservation, this leads to a gradual, average increase of the tube cross-section. To make possible analytical progress it is generally assumed that throughout the process the tube cross-section remains circular at all times; moreover, in order to prevent formation of singularities we also assume that this process is brought to a complete stop when parts of the magnetic tubular surface come into contact with one another. When the knot reaches its tightest configuration we regard this state as a final stage of the constrained relaxation process (see Fig. 1.20). In this idealised situation we expect to find a correspondence between different knot topologies and relative minimum energy levels.

This approach was initiated by Moffatt, who showed [31] that

$$M_{\min} = m \Phi^2 V^{-1/3}\ ; \tag{1.58}$$

here $M_{\min} > 0$ denotes the minimum value of the magnetic energy M, and $m = m(\mathcal{L}, h)$ a positive, dimensionless function of the topology of $\mathcal{L}$, and of the twist h. By assuming zero-framing for each link component ($h = 0$), we can establish [40] a correspondence with the topological crossing number $c_{\min}$ of $\mathcal{L}$, given by

$$m(\mathcal{L}, 0) = \left(\frac{2}{\pi}\right)^{1/3} c_{\min}\ . \tag{1.59}$$

As topological complexity grows with $c_{\min}$ the number of distinct knot types increases exponentially, so that (1.59) provides a rather loose information. A more

Fig. 1.20 Idealized magnetic relaxation of a trefoil knot and a Hopf link (image adapted from [44])

accurate relation can be found by using ropelength information [10]; this is defined for tight knots by

$$\lambda = \frac{L^*}{R^*} , \tag{1.60}$$

where the ropelength λ is given by the ratio of the knot minimal length L^* and its maximal cross-sectional radius R^*; λ is dimensionless. Since the tight unknot is represented by the fat torus, ropelength has a lower bound given by $\lambda_0 = 2\pi R^*/R^* = 2\pi$.

Following Chui and Moffatt [13], a precise analytical relation between ropelength and energy has been obtained by a constrained relaxation process [29]. For simplicity let's set $\Phi = 1$ and $V = 1$; from [44, 45], we have

$$M_{\min} = \frac{\lambda^{4/3}}{2\pi^{2/3}} + \frac{\pi^{4/3} h^2}{\lambda^{2/3}} . \tag{1.61}$$

Comparing (1.61) with (1.58), we can state that $M_{\min} = m(\mathcal{L}, h) = m(\lambda, h)$. Since the lowest energy levels are given by $h = 0$, we have

$$m(\lambda, 0) = \frac{\lambda^{4/3}}{2\pi^{2/3}} . \tag{1.62}$$

Using $\lambda_0 = 2\pi$ for the tight unknot, we have the absolute minimum given by $m_0 = (2\pi^2)^{1/3} \approx 2.70$; normalizing m with respect to this value, we get the non-dimensional value

$$\tilde{m} = \frac{m(\lambda, 0)}{m_0} = \left(\frac{\lambda}{2\pi}\right)^{4/3} , \tag{1.63}$$

which gives a direct relationship between the minimum energy level of a tight knot and its ropelength. The 4/3-power law was found also by Chui and Moffatt [13]. The relaxation process can also be interpreted in terms of dimensional arguments: considering the reduction in length $L \to pL$ by a positive factor $p < 1$, from volume conservation ($V = SL =$ constant) we have $S \to p^{-1}S$, and from the flux conservation we have $|\boldsymbol{B}| \to p|\boldsymbol{B}|$, which implies a quadratic reduction in the magnetic energy, i.e. $M \to p^2 M$. Moreover, under the assumption of circular cross-section, from the reduction of the cross-section S, we have $R \to p^{-1/2} R$, and $\lambda \to p^{3/2}\lambda$. Hence, from $p^2 = (p^{3/2})^{4/3}$, we must have $M \propto \lambda^{4/3}$.

When $h \neq 0$, the lowest energy levels are given by taking $\mathrm{d}M_{\min}/\mathrm{d}\lambda = 0$; from (1.61) we have $h = \lambda/\pi$, and therefore

$$M_{\min} = \frac{3}{2}\pi^{\frac{2}{3}} h^{\frac{4}{3}} \Phi^2 V^{-\frac{1}{3}} . \tag{1.64}$$

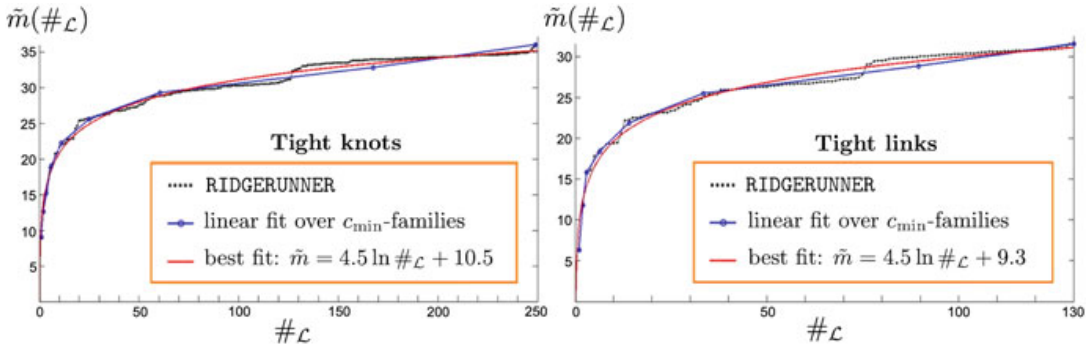

Fig. 1.21 Spectra of groundstate energy levels of prime tight knots (left) and links (right) given by plotting the non-dimensional energy $\tilde{m}$ against the position $\#_{\mathcal{L}}$ of the knot/link $\mathcal{L}$ ordered according to the increasing value of its ropelength λ (image adapted from [44])

In order to plot $\tilde{m}$ against the knot/link types, because the analytical relation of $\lambda = \lambda(\mathcal{L})$ is not known a priori, we rely on the numerical values of λ for each knot/link type obtained by the RIDGERUNNER tightening algorithm [2]. We take $\lambda(\mathcal{L}) = \lambda(\#_{\mathcal{L}})$, where $\#_{\mathcal{L}}$ refers to the position of a knot/link $\mathcal{L}$ ordered according to the increasing value of ropelength. The groundstate energy spectra of the first 250 prime knots (up to ten crossings), and 130 prime links (up to nine crossings), are shown in Fig. 1.21. The best-fit curves show an almost identical logarithmic behaviour, given by

$$\tilde{m} = 4.5 \ln \#_{\mathcal{L}} + C_{\mathcal{L}} \,, \tag{1.65}$$

where $C_{\mathcal{L}} = 10.5$ for knots, and $C_{\mathcal{L}} = 9.3$ for links. Similar energy-complexity relations hold for elastic knots, when we replace magnetic energy with bending energy [45].

1.4 Optimal Pathway in Knot Polynomial Space

In order to understand better the features of the untying pathway given by the cascade discussed in Sect. 1.2.5, we can take advantage of the numerical values associated with the adapted polynomials defined above, by introducing the concept of "knot polynomial space". This can be defined by considering the discrete set of numerical values given by the adapted polynomial for each knot type, so that a topological cascade of knots and links can be read in terms of these numerical values as points in an appropriate polynomial space. The actual topological cascade can thus be identified with a geodesic in this space. Consider for simplicity the first prime knots with $c_{\min} \leq 9$, and the adapted Jones polynomials of Sect. 1.2: in this case we have a one-to-one correspondence between knot types and Jones polynomials of positive exponent of highest degree n, so that each point of the space represents a unique knot type through its polynomial value.

1.4.1 Definition of a Knot Polynomial Space

We introduce the following definition [28] (see Fig. 1.22):

Definition 1.3 The knot polynomial space $\mathcal{V}_n^+$ is an n-dimensional, discrete, Euclidean space endowed by an Euclidean metric, whose isolated points (singletons) are the adapted Jones polynomials $V(\mathcal{L})$ up to the degree n.

In order to compute the geodesics, we must endow $\mathcal{V}_n^+$ with a metric; since each singleton is given by a knot polynomial, we can use orthogonal polynomials to construct a suitable metric. The Legendre polynomials $\{P_n(x)\}$ of degree n, with weight function unity and inner product defined over the finite interval $[-1, 1]$, are the simplest to satisfy the requirements. These are given by

$$P_0(x) = 1\,,\ P_1(x) = x\,,\ P_2(x) = \frac{1}{2}\left(3x^2 - 1\right)\,,\ P_3(x) = \frac{1}{2}\left(5x^3 - 3x\right)\,,\ \ldots\,,$$

with orthogonality condition given by

$$\langle P_n, P_m \rangle = \int_{-1}^{1} P_n\,(x)\,P_m\,(x)\,\mathrm{d}x = \frac{2}{2n+1}\delta_{nm}\,. \tag{1.66}$$

In order to have unit norm, we define

$$L_n(x) = \sqrt{\frac{2n+1}{2}}\,P_n(x)\,, \tag{1.67}$$

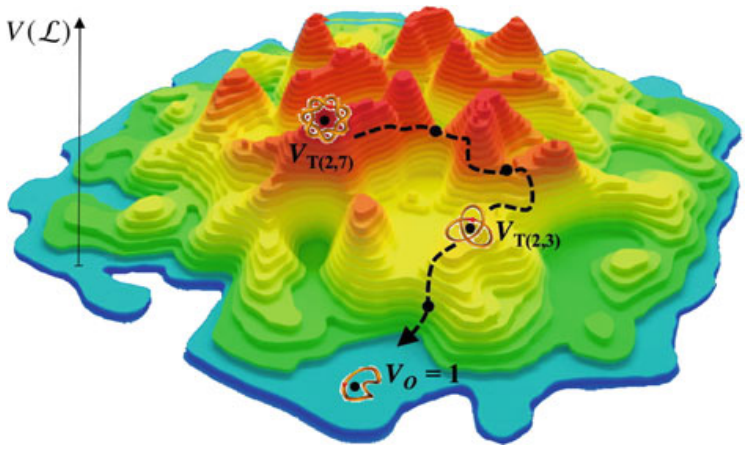

Fig. 1.22 A pictorial representation of the knot polynomial space $\mathcal{V}_n^+$, where each singleton (black dot) is represented by the (superposed) knot given by its Jones polynomial. Height is given by the adapted Jones polynomial value

so that (1.66) becomes

$$\langle L_n, L_m \rangle = \int_{-1}^{1} L_n(x)\, L_m(x)\, \mathrm{d}x = \delta_{nm} \,. \tag{1.68}$$

This endows $\mathcal{V}_n^+$ with Euclidean metric. We have:

Theorem 1.8 ([23]) *A polynomial $V(x)$ of degree n can be expanded into the first $n+1$ Legendre polynomials $L_0(x)$, $L_1(x)$, ..., $L_n(x)$, which provide a complete basis for the knot polynomial space $\mathcal{V}_n^+$.*

For physical applications (and for the sake of example) consider now the adapted Jones polynomial with $t^{1/2} = \mathrm{e}^{2\lambda_\omega Wr}$, $\langle Wr \rangle = 1/2$, and $\lambda_\omega \in [0, 1]$. Taking $x = t^{1/2}$, we have $x = \mathrm{e}^{\lambda_\omega} \in [1, \mathrm{e}]$. In order to use (1.68), we must transform the interval $[1, \mathrm{e}]$ into $[-1, 1]$; this is done by making a change of variable $x \to x'$, given by

$$x' = \frac{2}{\mathrm{e}-1} x - \frac{1+\mathrm{e}}{\mathrm{e}-1} \,, \tag{1.69}$$

so that

$$\int_1^{\mathrm{e}} f[V(x)]\, dx = \frac{2}{\mathrm{e}-1} \int_{-1}^{1} f[V(x')]\, \mathrm{d}x' \,. \tag{1.70}$$

Given the Euclidean metric defined by (1.68) we can compute the coordinates of a link $\mathcal{L}$ by identifying its adapted Jones polynomial $V(\mathcal{L})$ of degree n with the re-scaled Legendre polynomial $V_n(x')$; we thus have

$$V_{\mathcal{L}}(x') = c_0 L_0(x') + c_1 L_1(x') + \ldots + c_n L_n(x') \,, \tag{1.71}$$

where $V_{\mathcal{L}}(x') = V(x')$ is the Jones polynomial of degree n, whose coefficients (coordinates of $\mathcal{L}$) are given by

$$c_i = \int_{-1}^{1} V_{\mathcal{L}}(x') L_i(x')\, \mathrm{d}x' \,, \qquad (i = 0, \ldots, n) \,. \tag{1.72}$$

The geodesic distance between $\mathcal{L}_i$ and $\mathcal{L}_j$ can thus be defined by

$$d(V_{\mathcal{L}_j}, V_{\mathcal{L}_i}) = \| V_{\mathcal{L}_j} - V_{\mathcal{L}_i} \| = \sqrt{\frac{2}{\mathrm{e}-1}} \sqrt{\int_{-1}^{1} \left[V_{\mathcal{L}_j}(x') - V_{\mathcal{L}_i}(x') \right]^2 \mathrm{d}x'} \,. \tag{1.73}$$

Identifying the origin of the knot space with the unknot $\boldsymbol{U}_1$, the geodesic distance between $\mathcal{L}$ and $\boldsymbol{U}_1$ (where $V(\boldsymbol{U}_1) = 1$) is given by

$$d(\mathcal{L}, \boldsymbol{U}_1) = \left\| V_{\mathcal{L}} - V(\boldsymbol{U}_1) \right\| = \sqrt{\frac{2}{\mathrm{e}-1}} \sqrt{\int_{-1}^{1} \left[V_{\mathcal{K}}(x') - 1 \right]^2 \mathrm{d}x'} \,. \tag{1.74}$$

1.4.2 Unlinking Pathways in Knot Polynomial Space

The theory presented above can be applied to the case discussed in Sect. 1.2.5, and the data can be compared with those obtained by using different methods [50]. For this we must compute the probability associated with the unlinking pathways that brings the knot $T(2,6)$ to the unknot $T(2,1)$ ($\equiv \boldsymbol{U}_1$) by a series of successive, single, orientation preserving reconnection events that decrease topological complexity in a stepwise manner (see Fig. 1.23). The coordinates of the 11 knots/links considered are computed using Eq. (1.72) (see [28], Table 1); 17 different pathways Π_i ($i = 1, \ldots, 17$) are identified. With reference to Fig. 1.23, we have:

$$\Pi_1 : \quad T(2,6) \to T(2,5) \to T(2,4) \to T(2,3) \to T(2,2) \to T(2,1) \ ,$$

$$\Pi_2 : \quad T(2,6) \to T(2,5) \to D \to T(2,2) \to T(2,1) \ ,$$

$$\Pi_2 : \quad \ldots \ .$$

For each pathway Π_i we compute the total length d_i given by the algebraic sum of the intermediate distances between knot types along Π_i; for example, for the path

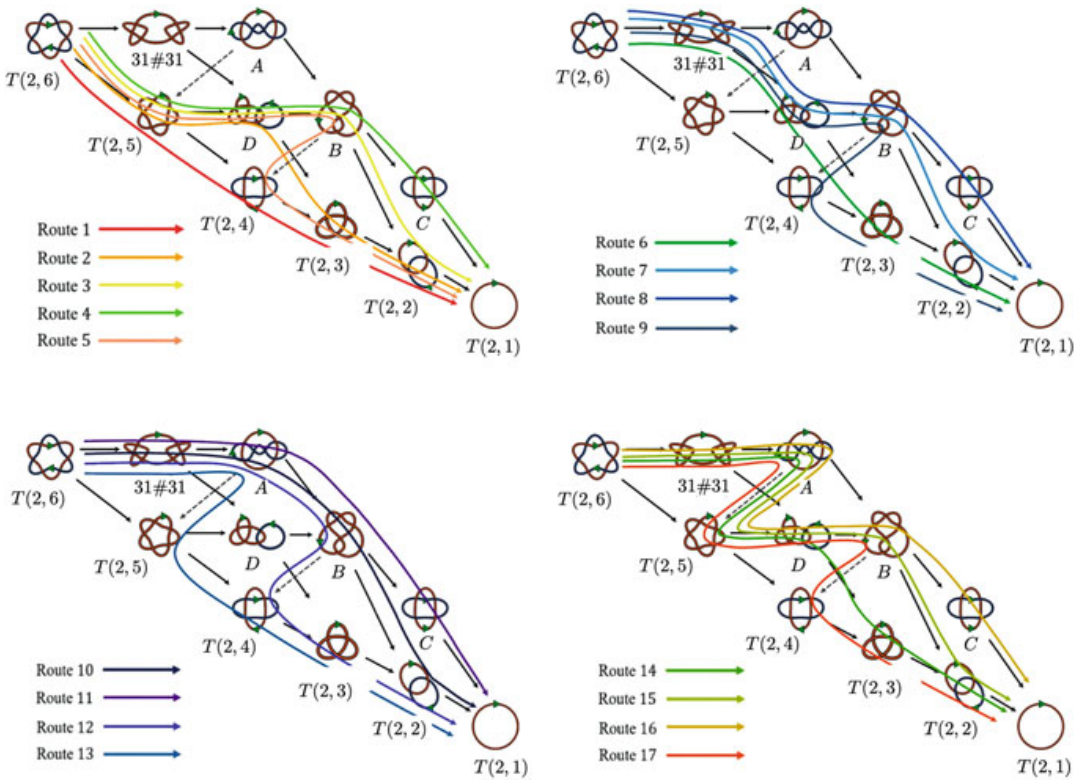

Fig. 1.23 Diagrammatic representation of the unlinking routes that bring the torus knot $T(2,6)$ to the unknot $T(2,1)$ by successive, single orientation preserving reconnections; 17 different pathways are identified (taken from [28] with permission)

Π_1 above, we have

$$d_1 = d[T(2,6), T(2,5)] + d[T(2,5), T(2,4)] + \ldots + d[T(2,2), T(2,1)] \, .$$

If we interpret the shortest path as the optimal route towards the unknot, pathway lengths can be related to the probability of occurrence by means of some simple definitions. For this let us define the direct path $\Pi_0 : T(2,6) \to T(2,1)$ of length $d_0 = d[T(2,6), T(2,1)]$, and determine the deviation of route Π_i from Π_0 by the relation

$$\sigma_i = \frac{d_i - d_0}{d_0} \, . \tag{1.75}$$

One simple definition of probability associated with the occurrence of the pathway Π_i is given by

$$p_i = \frac{\sigma_i^{-1}}{\sum_{i=1}^{17} \sigma_i^{-1}} \, , \tag{1.76}$$

which obviously satisfies the condition $\sum_{i=1}^{17} p_i = 1$. Direct computations show that the pathway Π_1 has the smallest deviation $\sigma_1 = 2.68 \times 10^{-4}$, and thus the highest probability of occurring $p_1 = 97.62\%$. It is interesting to note that the route Π_1 reproduces the cascade process pictorially represented by the sequence of Fig. 1.18. The monotone decrease of HOMFLYPT values (that can also be obtained in terms of Jones polynomials) is consistent with the present study. Route Π_{17} has the largest deviation $\sigma_{17} = 9.34 \times 10^{-1}$, thus the smallest probability to occur, $p_1 = 2.80\%$ (see Fig. 1.24). Direct comparison of the probability values obtained by [50] and by the method presented here, shown in Fig. 1.25, demonstrates the effectiveness of this new method.

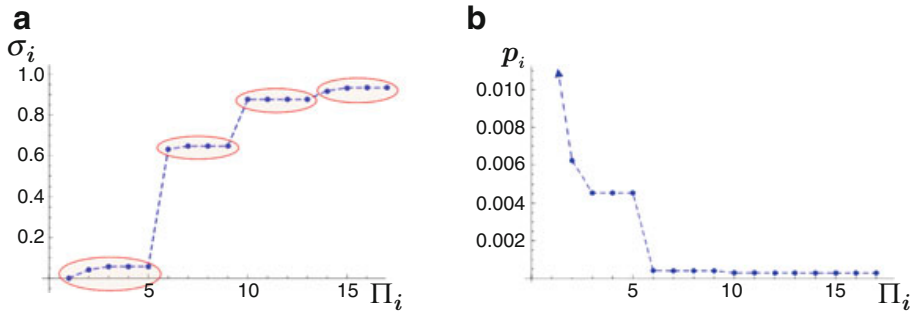

Fig. 1.24 (**a**) Deviation σ_i, and (**b**) probability p_i associated with each pathways Π_i ($i = 1, \cdots, 17$). Figure reproduced from [28] with permission

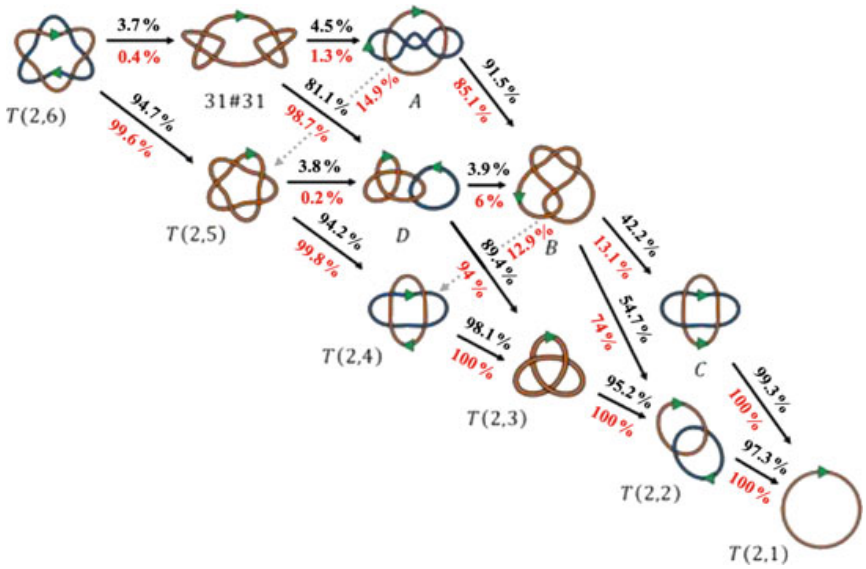

Fig. 1.25 Comparison of the relative probability values associated with each topological transition given in black by [50] with those given in red by [28]. Figure reproduced from [28] with permission

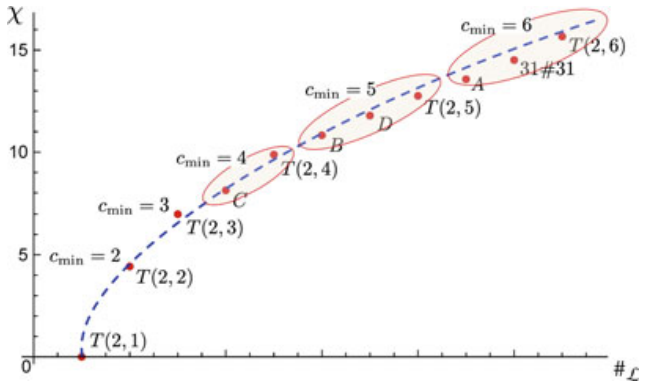

Fig. 1.26 Plot of χ against the ropelength position $\#_{\mathcal{L}}$ of the 11 knot/link types of the diagram of Fig. 1.25. The dashed, blue line represents the best-fit curve given by Eq. (1.78). The highlighted regions show the knots/links that have the same topological crossing number. Figure reproduced from [28] with permission

Using (1.74) we can introduce a new measure of topological complexity [28]:

Definition 1.4 The degree χ of topological complexity of a knot/link $\mathcal{L}$, is defined by

$$\chi(\mathcal{L}) = \ln\left[1 + d(\mathcal{L})\right]. \tag{1.77}$$

Figure 1.26 shows the plot of χ against the ropelength position $\#_{\mathcal{L}}$ of the 11 knot/link types of the diagram of Fig. 1.25. The highlighted regions show the

knots/links that have the same $c_{\min}$. A best-fit interpolation curve is given by the empirical relation

$$\chi(\mathcal{L}) = 6.3 \ln \#_{\mathcal{L}} - 0.13 \,. \tag{1.78}$$

This logarithmic behaviour (similar to that given by Eq. (1.65)) may admit physical interpretation in terms of some form of entropy. Defining the reconnection number $\#_{\text{rec}} = c_{\min} - 1$ as a lower bound to the number of single reconnections that reduce a given knot/link to the unknot, a logarithmic behaviour can be justified by relating the number of unlinking pathways (independent from the optimal geodesic) with the number $\#_{\text{rec}}$ associated with a given knot/link. Interpreting a topological change as a phase transition between different states, the observed cascade could then be interpreted as an expression of topological entropy in phase space.

1.5 Topological Cascade of Borromean Rings

To explore further aspects of topological cascade let us consider the evolution of three vortex rings forming a Borromean link $\boldsymbol{B}$ (see Fig. 1.6b). The topology of this link is rather complex, and represents a challenging example for our theory. For this let us consider the vortex rings given by defects in a Bose-Einstein condensate. Each vortex ring is defined by a nodal line γ_i $(i = 1, 2, 3)$ of a scalar, complex-valued wavefunction $\Psi = \Psi(\boldsymbol{x}, t)$ that governs a gas of particles (bosons), subject to a mean-field equation given by the Gross-Pitaevskii equation (GPE) [4, 37], that in non-dimensional form reads

$$\frac{\partial \Psi}{\partial t} = \frac{\mathrm{i}}{2} \nabla^2 \Psi + \frac{\mathrm{i}}{2} (1 - |\Psi|^2) \Psi \,, \tag{1.79}$$

where i denotes the imaginary unit and ∇^2 the Laplace operator. Under an appropriate transformation [4], this equation admits a hydrodynamic description in terms of a continuity and a momentum equation, given respectively by

$$\frac{\partial \rho}{\partial t} + \frac{\partial}{\partial x_i} (\rho u_i) = 0 \,, \tag{1.80}$$

$$\rho \Big(\frac{\partial u_i}{\partial t} + u_j \frac{\partial u_i}{\partial u_j} \Big) = - \frac{\partial p}{\partial x_i} + \frac{\partial \tau_{ij}}{\partial x_j} \,, \tag{1.81}$$

where $\rho = |\Psi|^2$ is the fluid density, $\boldsymbol{u} = u_i \hat{\boldsymbol{e}}_i = \nabla \theta$ the fluid velocity (where $\theta = \arg(\Psi)$), and $\tau_{ij} = (\partial^2 \ln \rho)/(4 \partial x_i \partial x_j)$ $(i, j = 1, 2, 3)$ the quantum stress tensor, function of the density gradients; everything is a smooth function of $\boldsymbol{x}$ and t. Each vortex is entirely localised on the nodal line, and it is characterised by a quantised circulation. The total energy of the system [4, 58] can be worked out from

the GPE Lagrangian, and it is given by

$$E = \frac{1}{2}\int \rho\,|\boldsymbol{u}|^2\,\mathrm{d}^3\boldsymbol{x} + \frac{1}{8}\int \frac{(\nabla\rho)^2}{\rho}\,\mathrm{d}^3\boldsymbol{x} - \frac{1}{2}\int \rho\,\mathrm{d}^3\boldsymbol{x} + \frac{1}{4}\int \rho^4\mathrm{d}^3\boldsymbol{x}\,, \tag{1.82}$$

where the integral terms above represent respectively the kinetic energy E_k, the quantum energy E_q, the potential energy E_p, and the internal energy E_i.

Starting from the Borromean link as the initial configuration, the three vortex rings evolve and interact with one another by a series of reconnections, and consequential change of topology. At length scales much larger than the typical vortex core size the vortex evolution is almost unaffected by the presence of the other vortices. When the relative separation distance is of the order of the vortex core size, each individual loop feels the presence of the other vortices, eventually comes into contact with the others, and the loops reconnect by a mutual exchange of vortex strands [22, 59].

1.5.1 Designing the Initial Condition

Conventionally, we set the vortex circulation equal to 2π, the fluid density $\rho \to 1$ as $\boldsymbol{x} \to \infty$, and the Mach number $M = \sqrt{2}$ (thus taking account of compressibility). Density is evaluated at each grid point by the minimum distance from the closest tangent according to the second-order Padé approximation [9]. If r denotes the radial distance from a point on the vortex line, we have a functional relation for the fluid density given by

$$\rho(r) \propto \frac{r^2\left(c_1 + c_2 r^2\right)}{1 + b_1 r^2 + c_2 r^4}\,, \tag{1.83}$$

where $c_1 = 11/32$, $b_1 = -1/7$ and $c_2 = c_1(b_1 - 1/4)$; higher-order approximations can also be used for higher accuracy.

For a given point P in space (but not on the vortex line) the wavefunction $\Psi(P)$ is computed in two steps:

(i) determine the nearest point $O \in \gamma_i$ $(i = 1, 2, 3)$ to P, define $r = \overline{OP}$, and use Eq. (1.83) to compute $\sqrt{\rho(r)} = |\Psi|$;
(ii) compute the angle θ between the unit normal at O and $\overrightarrow{OP}$, i.e. $\theta = \arg(\Psi)$ (see Fig. 1.27b).

In the case of the three Borromean rings, the resulting wavefunction at P is given by the three contributions from each individual wavefunction of the ring, i.e.

$$\Psi(P) = \Psi_1(P)\,\Psi_2(P)\,\Psi_3(P) = \sqrt{\rho_1\rho_2\rho_3}\,e^{\mathrm{i}(\theta_1+\theta_2+\theta_3)}. \tag{1.84}$$

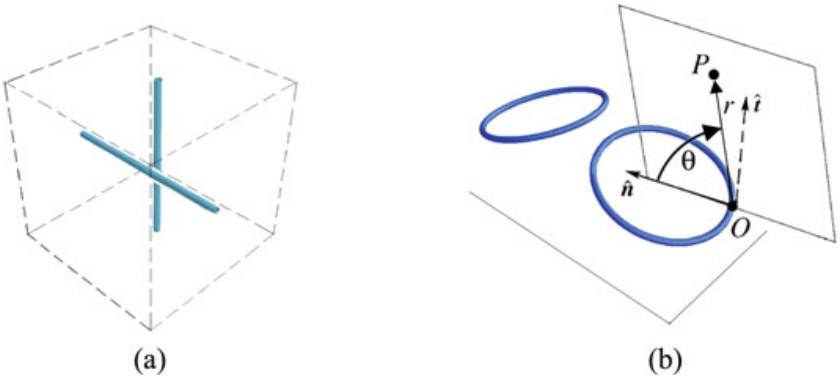

Fig. 1.27 (**a**) Two straight vortex segments, and (**b**) two vortex rings, with the plane defined by the unit normal at O and the position vector at the point P. The value of the wavefunctions at P is given by the superposition of the individual wavefunctions associated with each vortex

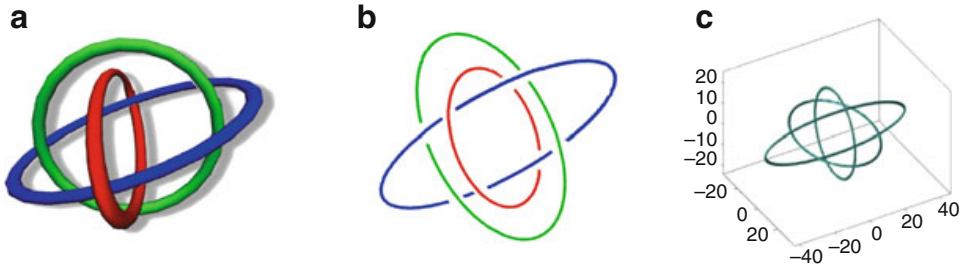

Fig. 1.28 (**a**) Pictorial representation of the Borromean rings in space; (**b**) initial configuration given by three planar ellipses, placed mutually orthogonal to one another; (**c**) representation of the initial configuration in the numerical box; vortex lines are visualised by iso-density tubular contours (where $\rho = 0.15$) centred on each nodal line γ_i ($i = 1, 2, 3$)

The initial configuration is given by taking three planar ellipses placed in mutually orthogonal planes as shown in Fig. 1.28b; in terms of vortex core size units, the geometry of the 3 ellipses is given by the following aspect ratios between major and minor axis: 60/40, 40/40, and 80/20. Numerically speaking, the only true, time-independent, exact solution to the GPE is given by the straight vortex line [11, 57].

The time evolution of the Borromean rings (hereafter denoted by $\boldsymbol{B}$ for short) is carried out by the numerical implementation of the GPE (1.79), prescribing the initial geometry and topology of the defects, and the computation of the energy contributions given by (1.82). This is done following the same methodology as in [59], using the Strang splitting method for time discretisation, while first and second space derivative operators are discretised by either fourth-order central finite differences, or one-sided finite differences according to the number of neighbouring points available. For the numerical simulation we set the following parameters:

- grid-points of the computational domain: $[-196; 36] \times [-44; 128] \times [-28; 120]$;
- vortex core size: $\xi = 1$;
- vortex circulation: $\Gamma = 2\pi$;

- spatial resolution: $\Delta x = \Delta y = \Delta z = 0.8\,\xi$;
- temporal resolution: $\Delta t = 1/80 = 0.0125$.

For technical details of the numerical method employed, see Caliari and Zuccher [11]. An improvement of this method can be found in [57].

1.5.2 Topological Cascade of the Borromean Rings

The Borromean rings undergo a sequence of orientation preserving, anti-parallel reconnections. The topology of the system changes, and several different unlinking pathways can be observed by changing the geometry of the initial configuration. One of the most recurrent pathways, however, is given by the initial production of a Whitehead link ($\boldsymbol{W}$), and the subsequent formation of a trefoil knot ($\boldsymbol{T}$), a Hopf link ($\boldsymbol{H}$), and several, disjoint unknotted loops ($\boldsymbol{U}_N$) (see Fig. 1.29). The observed transition from the Whitehead link (a 5-crossing link type) to a trefoil knot provides an example of direct topological collapse [58] with the instantaneous unlinking of 2 crossings. This transformation is not entirely unexpected, since it is similar to the decay of the 5-crossing D-link to the trefoil knot represented by the diagram of Fig. 1.25. As mentioned, this pattern is not unique, but it represents one of the most probable decay paths observed.

Under GPE evolution total mass and energy are both quantities conserved in time. A detailed numerical inspection of the energy terms of Eq. (1.82) shows that major changes affect the kinetic and internal energy, whereas the changes of potential energy (essentially related to the total mass), and quantum energy remain essentially negligible throughout the evolution. Focus is therefore put on the change of kinetic energy E_k, which is almost entirely compensated by a change of internal energy E_i. In the diagram of Fig. 1.30 we report a preliminary summary of this process, plotting the internal energy change against the simulation time for the vortex evolution.

We account for a total relative variation $\Delta E_i / E_i$ of the order of 1%. The initial and the final intervals (denoted by the white areas in the diagram), are both of the order of 5% of the total simulation time (300 units); since these do not provide accurate information because of the numerical errors caused by the periodicity of the numerical box, they are not taken into account for quantitative analysis. The five regions of different colours correspond to the key topological states shown in Fig. 1.29, which are reproduced by the snapshots shown on the top row of Fig. 1.30. The horizontal dashed lines represent the average value of ΔE_i of each topological type.

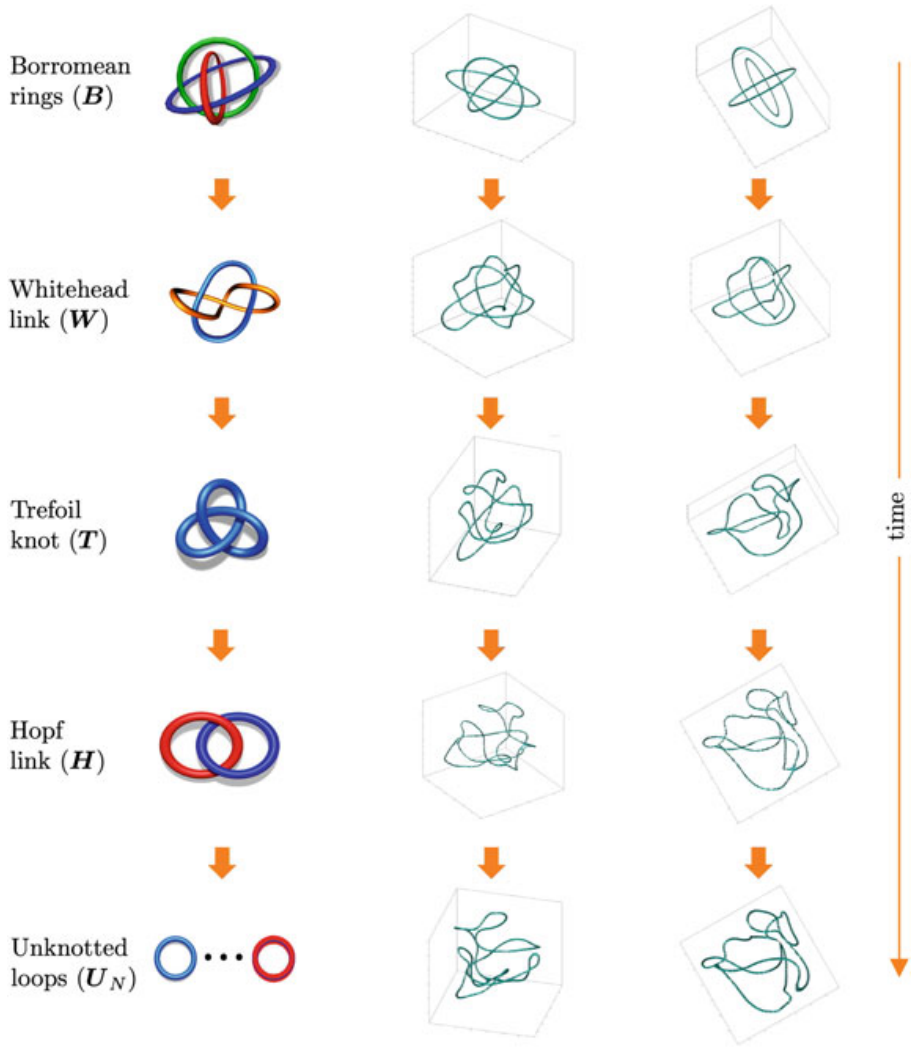

Fig. 1.29 (Left column) Pictorial representation of the topological states observed during the time evolution of the Borromean vortex rings after subsequent anti-parallel reconnections. (Centre and right columns) Snapshots of the numerical simulation of the actual vortex loops seen from different viewing angles. The 6-crossing Borromean rings ($\boldsymbol{B}$) are seen to decay to form a 5-crossing Whitehead link ($\boldsymbol{W}$), then a trefoil knot ($\boldsymbol{T}$), a negative Hopf link ($\boldsymbol{H}$), and several, disjoint unknotted loops ($\boldsymbol{U}_N$)

After an initial apparent drop of internal energy due to the neglected transient time, we observe a gradual increase of the average internal energy of the system, that corresponds to a continuous decrease of kinetic energy. Since the process involves repeated reconnections, part of the observed change of internal energy can be ascribed to the occurrence of these events. The marked increase of ΔE_i in the last stage of the process may be due to the final production of several unknotted loops. Work is in progress to analyse in greater detail the huge amount of information provided by this complex process.

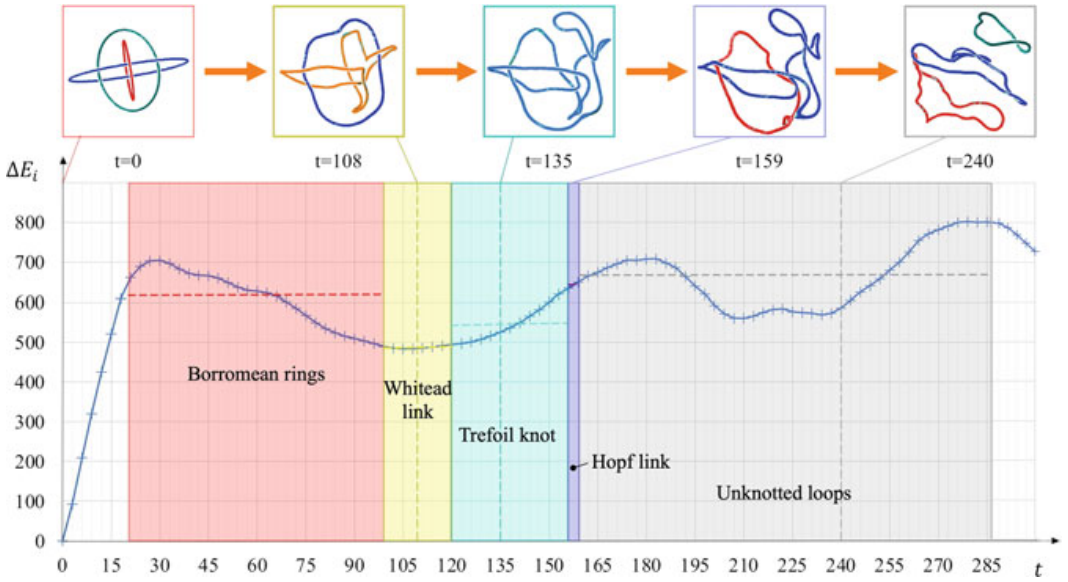

Fig. 1.30 Change of interaction energy of decaying Borromean rings plotted against time (sequence of topological states represented by the vortex centrelines on top). The initial ($t \in [0, 21]$) and final stage ($t \in [285, 300]$) of the plot (delimited by a dashed, black line) are not considered because affected by numerical errors. Interaction energy average values are denoted by horizontal lines adjustments of the wavefunction

Acknowledgments X.L. and R.L.R. wish to acknowledge financial support from the Beijing Natural Science Foundation (grants n. IS23030, Z180007) and the National Natural Science Foundation of China (grant n. 11572005). H.G. wishes to acknowledge financial support from the China Scholarship Council (grant n. 202106540044).

References

1. Arnold, V.I., Khesin, B.A.: Topological Methods in Hydrodynamics. Springer-Verlag, Berlin (1998)
2. Ashton, T., Cantarella, J., Piatek, M., Rawdon, E.: Knot tightening by constrained gradient descent. Exp. Math. **20**, 57–90 (2011)
3. Atiyah, M.: The Geometry and Physics of Knots. Cambridge University Press, Cambridge (1990)
4. Barenghi, C.F., Parker, N.G.: A Primer of Quantum Fluids. Springer-Verlag, Berlin (2016)
5. Barenghi, C.F., Ricca, R.L., Samuels, D.C.: How tangled is a tangle? Physica D **157**, 197–206 (2001)
6. Belloni, A., Ricca, R.L.: On the zero helicity condition for quantum vortex defects. J. Fluid Mech. **963**, R2 (2023)
7. Berger, M.A.: An energy formula for nonlinear force-free magnetic fields. Astron. Astrophys. **201**, 355–361 (1988)
8. Berger, M.A., Field, G.B.: The topological properties of magnetic helicity. J. Fluid Mech. **147**, 133–148 (1984)
9. Berloff, N.G.: Padé approximations of solitary wave solutions of the Gross-Pitaevskii equation. J. Phys. A Math. Theor. **37**, 1617–1632 (2004)
10. Buck, G., Simon, J.: Thickness and crossing number of knots. Topol. Appl. **91**, 245–257 (1999)

11. Caliari, M., Zuccher, S.: Reliability of the time splitting Fourier method for singular solutions in quantum fluids. Comput. Phys. Commun. **222**, 46–58 (2018)
12. Călugăreanu, G.: Sur les classes d'isotopie des noeuds tridimensionnels et leurs invariants. Czech Math. J. **11**, 588–625 (1961)
13. Chui, A.Y.K., Moffatt, H.K.: The energy and helicity of knotted magnetic flux tubes. Proc. R. Soc. Lond. A **451**, 609–629 (1995)
14. Duan, Y.-S., Liu, X., Zhang, P.-M.: Decomposition theory of the $U(1)$ gauge potential and the London assumption in topological quantum mechanics. J. Phys. Cond. Matter **14**, 7941–7947 (2002)
15. Elhamdadi, M., Hajij, M., Istvan, K.: Framed knots. The Math. Intell. **42**, 7–22 (2020)
16. Freyd, P., Yetter, D., Hoste, J., Lickorish, W.B.R., Millett, K., Ocneanu, A.: A new polynomial invariant of knots and links. Bull. Am. Math. Soc. **12**, 239–246 (1985)
17. Jones, V.F.R.: Hecke algebra representations of braid groups and link polynomials. Ann. Math. **126**, 335–388 (1987)
18. Kauffman, L.H.: On Knots. Princeton University Press, Princeton (1987)
19. Kauffman, L.H.: Knots and Physics. World Scientific, Singapore (2001)
20. Kleckner, D., Irvine, W.T.M.: Creation and dynamics of knotted vortices. Nature Phys. **9**, 253–258 (2013)
21. Kleckner, D., Kauffman, L.H., Irvine, W.T.M.: How superfluid vortex knots untie. Nature Phys. **12**, 650–655 (2016)
22. Koplik, J., Levine, H.: Vortex reconnection in superfluid helium. Phys. Rev. Lett. **71**, 1375–1378 (1993)
23. Leon, S.: Linear Algebra with Applications. Pearson, Prentice Hall, Upper Saddle River (2010)
24. Lickorish, W.B.R., Millett, K.C.: The new polynomial invariants of knots and links. Math. Mag. **61**, 3–23 (1988)
25. Liu, X., Ricca, R.L.: The Jones polynomial for fluid knots from helicity. J. Phys. A Math. Theor. **45**, 205501 (2012)
26. Liu, X., Ricca, R.L.: On the derivation of the HOMFLYPT polynomial invariant for fluid knots. J. Fluid Mech. **773**, 34–48 (2015)
27. Liu, X., Ricca, R.L.: Knots cascade detected by a monotonically decreasing sequence of values. Sci. Rep. **6**, 24118 (2016)
28. Liu, X., Ricca, R.L., Li, X.: Minimal unlinking pathways as geodesics in knot polynomial space. Commun. Phys. **3**, 136 (2020)
29. Maggioni, F., Ricca, R.L.: On the groundstate energy of tight knots. Proc. R. Soc. A **465**, 2761 (2009)
30. Moffatt, H.K.: The degree of knottedness of tangled vortex lines. J. Fluid Mech. **35**, 117–129 (1969)
31. Moffatt, H.K.: The energy spectrum of knots and links. Nature **347**, 367–369 (1990)
32. Moffatt, H.K.: Helicity and singular structures in fluid dynamics. Proc. Natl. Acad. Sci. USA **111**, 3663–3670 (2014)
33. Moffatt, H.K.: Helicity invariant even in a viscous fluid. Science **357**, 6350 (2017)
34. Moffatt, H.K., Ricca, R.L.: Helicity and the Călugăreanu invariant. Proc. R. Soc. A **439**, 411–429 (1992)
35. Moreau, J.J.: Constantes d'un îlot tourbillonnaire en fluid parfait barotrope. C. R. Acad. Sci. Paris **252**, 2810–2812 (1961)
36. Oberti, C., Ricca, R.L.: Energy and helicity of magnetic torus knots and braids. Fluid Dyn. Res. **50**, 011413 (2018)
37. Pitaevskii, L.P., Stringari, S.: Bose-Einstein Condensation. International Series of Monographs on Physics. Oxford University Press, Oxford (2003)
38. Przytycki, J.H., Traczyk, P.: Conway algebras and skein equivalence of links. Proc. Am. Math. Soc. **100**, 744–748 (1987)
39. Reidemeister, K.: Elementare Begründung der Knotentheorie. Abh. Math. Sem. Univ. Hamburg **5**, 24–32 (1927)
40. Ricca, R.L.: Topology bounds energy of knots and links. Proc. R. Soc. A **464**, 293–300 (2008)

41. Ricca, R.L., Liu, X.: The Jones polynomial as a new invariant of topological fluid dynamics. Fluid Dyn. Res. **46**, 061412 (2014)
42. Ricca, R.L., Liu, X.: HOMFLYPT polynomial is the best quantifier for topological cascades of vortex knots. Fluid Dyn. Res. **50**, 011404 (2018)
43. Ricca, R.L., Moffatt, H.K.: The helicity of a knotted vortex filament. In: Moffatt, H.K. et al. (eds.) Topological Aspects of the Dynamics of Fluids and Plasmas, pp. 225–236. Kluwer Academic, Amsterdam (1992)
44. Ricca, R.L., Maggioni, F.: On the groundstate energy spectrum of magnetic knots and links. J. Phys. A Math Theor **47**, 205501 (2014)
45. Ricca, R.L., Maggioni, F.: Groundstate energy spectra of knots and links: magnetic versus bending energy. In: Blatt, S., Reiter, P., Schikorra, A. (eds.) New Directions in Geometric and Applied Knot Theory. OA Measure Theory, pp. 276–288. De Gruyter, Basel (2018)
46. Ricca, R.L., Nipoti, B.: Gauss' linking number revisited. J. Knot Theory Its Ram. **20**, 1325–1343 (2011)
47. Russell, A.J.B., Yeates, A.R., Hornig, G., Wilmot-Smith, A.L.: Evolution of field line helicity during magnetic reconnection. Phys. Plasmas **22**, 032106 (2015)
48. Scheeler, M.W., van Rees, W.M., Kedia, H., Kleckner, D., Irvine, W.T.M.: Complete measurement of helicity and its dynamics in vortex tubes. Science **357**, 487–491 (2017)
49. Shimokawa, K., Ishihara, K., Grainge, I., Sherratt, D.J., Vazquez, M.: FtsK-dependent XerCD-dif recombination unlinks replication catenanes in a stepwise manner. Proc. Natl. Acad. Sci. USA **110**, 20906 (2013)
50. Stolz, R., Yoshida, M., Brasher, R., Flanner, M., Ishihara, K., Sherratt, D.J., Shimokawa, K., Vazquez, M.: Pathways of DNA unlinking: a story of stepwise simplification. Sci. Rep. **7**, 12420 (2017)
51. Sumners, De W.L., Cruz-White, I.I., Ricca, R.L.: Zero helicity of Seifert framed defects. J. Phys. A: Math. Theor. **54**, 295203 (2021)
52. Thomson, W. (Lord Kelvin): On vortex motion. Trans. R. Soc. Edin. **25**, 217–260 (1868)
53. White, J.H.: Self-linking and the Gauss integral in higher dimensions. Am. J. Math. **91**, 693–728 (1969)
54. Witten, E.: Quantum field theory and the Jones polynomial. Commun. Math. Phys. **121** 351–399 (1989)
55. Woltjer, L.: A theorem on force-free magnetic fields. Proc. Natl. Acad. Sci. USA **44**, 489–491 (1958)
56. Xiong, S., Yang, Y.: Construction of knotted vortex tubes with the writhe-dependent helicity. Phys. Fluids **31**, 047101 (2019)
57. Zuccher, S., Caliari, M.: Accurate numerical determination of a self-preserving quantum vortex ring. J. Phys. A Math. Theor. **54**, 015301 (2021)
58. Zuccher, S., Ricca, R.L.: Creation of quantum knots and links driven by minimal surfaces. J. Fluid Mech. **942**, A8 (2022)
59. Zuccher, S., Caliari, M., Baggaley, A.W., Barenghi, C.F.: Quantum vortex reconnections. Phys Fluids **24**, 125108 (2012)